

# The use of locally resonant metamaterials to reduce flow-induced noise and vibration

F.A. Pires<sup>a,b,\*</sup>, L. Sangiuliano<sup>a,b</sup>, H. Denayer<sup>a,b</sup>, E. Deckers<sup>b,c</sup>, W. Desmet<sup>a,b</sup>, C. Claeys<sup>a,b</sup>

<sup>a</sup>*KU Leuven, Department of Mechanical Engineering, Division LMSD, Celestijnenlaan 300-box 2420, 3001 Heverlee, Belgium*

<sup>b</sup>*DMMS Lab, Flanders Make, Belgium*

<sup>c</sup>*KU Leuven, Diepenbeek Campus, Mechanical Engineering Technology TC, Wetenschapspark 27, 3590 Diepenbeek, Belgium*

5

---

## Abstract

Locally resonant metamaterials (LRMs) have recently emerged and shown potential in the field of noise control engineering, given their superior noise and vibration reduction performance in tunable frequency ranges, referred to as stop bands. This paper aims to experimentally assess the potential of LRMs to suppress flow-induced noise and vibration of coupled vibro-acoustic systems such as a cavity-backed plate. At first, the vibrations of a flat plate under a turbulent flow excitation are measured and analyzed. Subsequently, different LRM solutions are designed to tackle the vibrations of the plate. In a second stage, a hard-walled backing-cavity is coupled to the system and the noise radiation due to the vibrations of the plate into the backing cavity is evaluated. The plate is then treated with the designed LRM configurations. The results show that the designed LRM solutions are able to reduce the vibrations and noise radiation of the system due to a turbulent flow excitation.

*Keywords:* Locally resonant metamaterials, Stop bands, Flow-induced noise and vibration, Vibro-acoustic systems

10

---

## 1. Introduction

In the past years, the mitigation of flow-induced vibration and the associated noise has gained importance with the goal of reducing the noise levels and improving the comfort in vehicle and aircraft cabins [1–3]. For instance, in the automotive sector, the vibrations found on the underbody of a moving car are induced by an unsteady turbulent flow, which leads to unsteady pressure loads on the floor of the vehicle, causing noise to be radiated into the cabin of the car. Similarly, for an aircraft, the turbulent boundary layer (TBL) developing

15

---

\*KU Leuven, Department of Mechanical Engineering, Division LMSD, Celestijnenlaan 300-box 2420, 3001 Heverlee, Belgium.

*Email addresses:* felipe.alvespires@kuleuven.be (F.A. Pires), luca.sangiuliano@kuleuven.be (L. Sangiuliano), herve.denayer@kuleuven.be (H. Denayer), elke.deckers@kuleuven.be (E. Deckers), wim.desmet@kuleuven.be (W. Desmet), claus.claeys@kuleuven.be (C. Claeys)

over the fuselage causes pressure fluctuations that can excite structural vibrations as well as noise, which can be transmitted through the fuselage and radiate into the cabin, affecting directly the comfort of passengers [4]. For such applications, flow-induced noise and vibration are typically a low frequency problem, where the highest energy content is present below 1000 Hz [5, 6].

A variety of studies have been developed to obtain a good prediction of these pressure loads in order to characterize this Noise, Vibration and Harshness (NVH) behavior [7–10]. For example, in the work of Klabes (2017) [7], a tool chain is developed to estimate the vibrations of an aircraft fuselage at cruise flight conditions, in which Computational Fluid Dynamics (CFD) and various semi-empirical approaches are used to calculate the TBL excitation, while in the study of Marchetto (2017) [9], a methodology is developed to characterize the structural response of flat plates under TBL excitation without conventional measurement techniques such as a wind tunnel. The approach is based on separating the contributions of the forcing excitation and those of the dynamic behavior of the structure. The methodology is shown to give a good estimation of the vibrational response when compared with direct measurements in an anechoic wind tunnel.

Apart from the TBL-induced phenomena, the effects of a turbulent flow around bluff bodies are also of significant importance [11]. For a bluff cylinder, as a result of boundary layer roll-up, alternating vortices are created and shed, which continue to grow under continuous injection of circulation from the cylinder shear layers until they become strong enough to draw the shear layers across the wake [12]. These vortices stop building up in strength and shed away from the cylinder as the vorticity with an opposite sign in sufficient concentration cuts further supply of circulation to the forming vortex [13]. This phenomenon can have tonal as well as broadband characteristics for low and high Reynolds numbers, respectively, and is often referred to as vortex-shedding [14]. A practical problem of this phenomenon may be, for example, when the turbulent flow finds a bluff component on the underbody of a moving car or even a luggage rack on its roof, which can generate greater noise levels inside the car’s cabin.

Different solutions to mitigate flow-induced noise and vibration have been studied and developed: from the addition of mass and/or modifications on the system’s stiffness to the use of damping layers as well as active control approaches [15–17]. For example, in the study of Graham (1996) [15], some passive techniques are applied and investigated on a simply supported elastic plate, representing a fuselage of an aircraft, under a boundary layer excitation. The authors found that increasing the structural damping and decreasing the skin stiffness and number of reinforcements can reduce the radiated sound of the fuselage. While in Barton (1981) [16], the addition of mass and skin stiffness are assessed and applied to an aircraft fuselage. The authors indicated that adding either mass or stiffness to the fuselage skin can improve the sidewall attenuation and that a honeycomb stiffness treatment provided more improvement at most frequencies than an equal amount of added mass. In Maury et al. (2001) [17], an active control approach is applied to reduce the flow-induced noise transmitted through a plate. The used active control strategy was able to attenuate the sound power radiated by the structure by suppressing specific radiation modes up to 1 kHz. However, passive countermeasures often lead to heavy as well as bulky NVH solutions

and may not perform desirably in the lower frequency range [18]. Active solutions may work well at lower frequencies, however, these are more demanding to implement, typically more expensive and always require energy supply.

Among potential solution techniques to tackle the low frequency range, the approach of applying multiple resonant elements to an elastic host structure has been largely investigated, for which the potential of creating an apparent damping effect induced by an optimal tuning of the attached resonators is typically of interest [19–23]. In this case, the damping effect relies on the the net force that the non-nominally equal tuned resonant additions exert back on the primary structure as they start to oscillate and not on the classical energy dissipation mechanisms. Such approach offers the benefit of achieving a superior vibration insulation over broader frequency ranges due to the strategic frequency distribution of the resonators. For example, in the work of Koç et al. (2005) [21], a study is performed on an energy trapping concept for vibration attenuation. The authors concluded that a set of resonant elements can collectively absorb and retain vibratory energy for a particular distribution of their natural frequencies. In the work of Carcaterra et al. (2012) [22], a shock absorbing device for aerospace practical applications that consists of a set of optimally detuned resonators that absorb the vibration energy of a primary structure is developed. The results show that the device is effective to reduce the vibrations within the desired frequency ranges. Albeit such technique does not require a fine-tuning of resonators and offers the benefit of achieving a superior vibration insulation over broader frequency ranges due to the strategic frequency distribution of the resonators, this typically occurs at the expense of reducing the peak attenuation of vibrations at a targeted (tonal) frequency since, for this case, several frequencies are targeted instead of one. Besides, when the multiple resonant elements are only added at one location, as for example in the work of Carcaterra et al. (2012) [22], possibly only local vibration reduction is achieved in the case of large structures with distributed excitation. When multiple of these multi-resonant structures are added to a structure, the solution might become rather heavy and large, which can constrain the application of the solution, depending on the available installation space at the desired location. Besides, a trade-off between peak performance at a tonal frequency and broadband reduction often needs to be made. Thus, in the context of flow-induced noise and vibration, where tonal issues often occur and achieving a more global vibration reduction over the entire net area of the structure can be of interest, innovative solutions are required to tackle the conflicting requirements of achieving a good NVH reduction performance at low (tonal) frequencies as well as a lightweight and compact design.

Recently, LRMs have proven to be good candidates to tackle (tonal) frequencies at the low frequency range by combining a lightweight and compact design and superior peak attenuation performance with an excellent global vibration reduction over the structure of interest in desired frequency regions, known as stop bands. They are frequency zones where free wave propagation is not allowed [24] and can be created by the addition of nominally equal tuned (fine-tuned) resonators to an elastic host structure on a subwavelength scale i.e. on a scale much smaller than the wavelength of the targeted structural waves [25, 26]. In LRMs, the stop band creation is due to a Fano-type interference [27, 28]. Stop bands are typically predicted by the computation of dispersion diagrams, which can be calculated

105 by unit cell (UC) modeling, using a finite element (FE) model in combination with the Bloch-Floquet theorem [29, 30].

LRM concepts have been designed and experimentally investigated for several engineering applications, covering a wide range of vibro-acoustic excitation mechanisms [31–34]. On the one hand, several studies are performed using a structural excitation by a point force, such as impact hammer. For example, in Wu et al. (2008) [31], a LRM plate is studied and excited by a pulsed laser fixed in one point on the host to generate broadband elastic waves. In the study of Jung et al. (2019) [32], resonators are attached to an automobile dash panel, in which both structural and noise radiation responses are evaluated when excited by an impact hammer. On the other hand, some studies are carried out by utilizing an acoustic source. In the study of Hall (2017) [33], the diffuse field sound transmission loss (STL) of gypsum plasterboard and aluminum panels, respectively, with periodically attached beam-shaped resonators was measured. In the work of Filho et al. (2020) [34], the acoustic insulation of LRM double-panel partitions with a foam core is evaluated. Nevertheless, these works do not carry out any assessment on the LRM reduction performance in structures under an aerodynamic excitation. In Wang et al. (2017) [35], an analytical study is performed to predict the STL of a LRM plate under the influence of an external mean flow. The authors found that as the Mach number increases, it helps to achieve higher STL below the coincidence frequency but impairs the system’s acoustic insulation above coincidence. However, given that the analytical model in study is homogenized, it does not take into account the fact that significant pressure fluctuations may occur while a turbulent flow excites the system. Besides, an experimental verification that LRMs can work in such conditions is not provided.

For this reason, the present paper proposes to experimentally investigate the potential of LRMs to improve flow-induced noise and vibration insulation in the lower frequency range below 1000 Hz. This investigation is performed by analyzing the vibrations of a flat plate and, subsequently, its sound radiation into a hard-walled backing-cavity coupled to it, for different flow conditions. Different LRM solutions are designed, produced and tested to assess the vibro-acoustic performance of the system excited by a grazing flow and a flow over a bluff obstacle.

135 The paper is organized as follows. In section 2, the types of flow excitation and the vibro-acoustic system used in the work are introduced. Section 3 presents the LRM designs and the methodology for the stop band prediction, which makes use of UC modeling. In section 4, the experimental results regarding the use of LRMs to reduce flow-induced noise and vibration of a cavity-backed plate are presented and analyzed. Lastly, section 5 summarizes the main findings of this paper.

## 2. Problem definition

In this section, firstly, the test set-up configurations is introduced. Subsequently, the characteristics of the flow conditions used to excite the system are analyzed. Lastly, the vibro-acoustic system used in the work to investigate the application of LRMs to reduce flow-induced noise and vibration is introduced and its bare responses evaluated.

## 2.1. Test configurations

The presence of flow can lead to different types of NVH issues, thus, studying the potential of LRMs to target different flow conditions is important. Two flow phenomena are studied in this work for which a LRM solution is applied: (i) a TBL excitation and (ii) vortex-shedding in a wake of a bluff body, exciting the system. 150

To perform the study, this work uses a test-rig that consists of a small wind tunnel formed by aluminum duct sections, and built in connection with two roots blowers added in parallel, which can provide constant air flow rates [36]. The flow is led through an aftercooler to ensure nearly constant conditions for the tests.

Two set-up configurations are utilized in the investigation, which are placed on a side-wall of a test duct section with cross-sectional dimensions  $150 \times 75$  mm: (i) a flexible flat plate and (ii) a cavity-backed plate, as illustrated in Figure 1 a) and b). Information about the characteristics of the systems is given in the next sections. 155

In the same duct section, the flexible plate can be replaced by a rigid wall containing an array of microphones while keeping the same position in the set-up, as shown in Figure 1 c). 160 The latter configuration is used in this work in order to have an estimation of the flow characteristics for the considered aerodynamic loads over the flexible flat plate. This strategy is a good and faster alternative to using CFD and/or semi-empirical approaches to estimate the pressure loads for the application in study since it is not computationally demanding and can give a very good approximation of the aerodynamic excitation in reality. The grid 165 spacing between each microphone is 30 mm in the x and y directions, which is chosen to be subwavelength with respect to the structural wavelength for the considered structure at 1000 Hz. However, in order to have a more detailed information about the aerodynamic characteristics of the excitation, a finer grid of microphones is needed, but since it is out of the scope of this work, this is not done. 170

In this paper, mainly two quantities are used to evaluate the noise and vibration behavior of the systems, namely, the power spectral density (PSD) autopower of pressure and velocity, respectively. The PSD autopowers are computed from the measured time signal by using the Welch's method [37] for a frequency resolution  $\Delta f = 1$  Hz, with 150 averages and Hanning window [38] applied with 25% overlap. 175

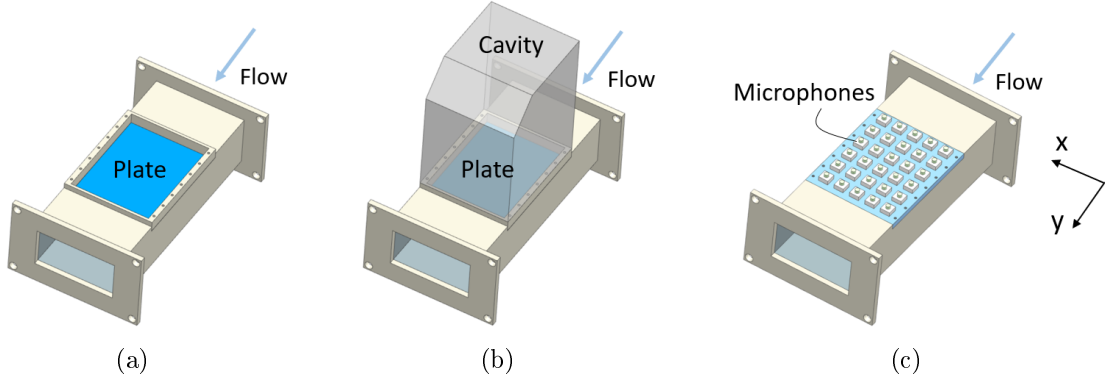


Figure 1: Schematic illustration of the test duct section containing the a) flat plate, b) cavity-backed plate and c) array of microphones.

For the grazing flow excitation, a flow of air with different average flow speeds is used: (i)  $U^{(1)} = 9$  m/s (ii)  $U^{(2)} = 14$  m/s and (iii)  $U^{(3)} = 19$  m/s. These average speeds are calculated based on the measured flow rates by a flow meter mounted in the test-rig for a location in which the cross-sectional area is constant for a length of 2 meters, namely  $Q^{(1)} = 370$  m<sup>3</sup>/h,  $Q^{(2)} = 570$  m<sup>3</sup>/h and  $Q^{(3)} = 770$  m<sup>3</sup>/h and a cross-section of  $150 \times 75$  mm. The density and viscosity of the air are considered to be  $\rho_{air} = 1.225$  kg/m<sup>3</sup> and  $\mu_{air} = 1.78 \cdot 10^{-5}$  Pa.s, respectively. The used flow speeds correspond to the Reynolds numbers  $Re^{(1)} = 1.2 \cdot 10^6$ ,  $Re^{(2)} = 1.9 \cdot 10^6$  and  $Re^{(3)} = 2.6 \cdot 10^6$  as well as Mach numbers  $M^{(1)} = 0.027$ ,  $M^{(2)} = 0.041$  and  $M^{(3)} = 0.056$ , respectively. These Reynolds number calculations are performed in order to have an indication of the flow turbulent state while exciting the system.

To evaluate the behavior of the system excited by the wake of a bluff object in the flow, this work takes the approach of keeping a fixed flow speed and adding bluff cylinders in the flow stream. This work uses  $U^{(3)} = 19$  m/s as the reference speed for the excitation by the turbulent wake. Three different diameters of cylinders of length 150 mm are used in order to experimentally verify whether this can lead to an increased vibro-acoustic excitation in different frequency regions: (i)  $D_1 = 5$  mm, (ii)  $D_2 = 6$  mm and (iii)  $D_3 = 8$  mm. In order to have an indication of the shedding that each bluff object may produce, the Reynolds number for each case are also calculated:  $Re_s^{(1)} = 6.6 \cdot 10^3$ ,  $Re_s^{(2)} = 7.9 \cdot 10^3$  and  $Re_s^{(3)} = 1.1 \cdot 10^4$ . Figure 2 illustrates how the cylinder is attached to the system. The cylinders are positioned at a distance close enough to the top duct wall, so that the turbulent wake can hit this surface. The cylinders are glued at a distance  $h \approx D_c$  from the top wall.

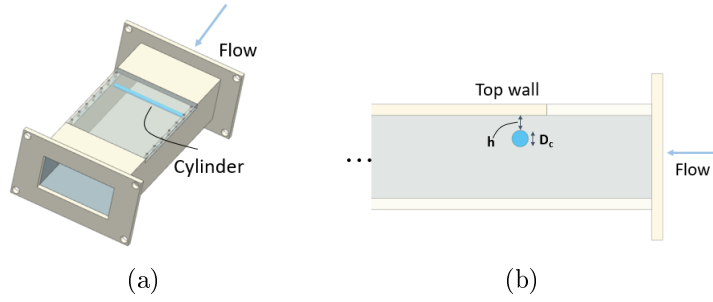


Figure 2: Schematic representation of a) cylindrical rod inside the duct and b) side-view of the duct with a cylindrical rod.

### 2.1.1. Grazing flow pressure fluctuations

In order to have an indication of the characteristics of the excitation for the flow configurations studied in this work, the pressure fluctuations for each flow condition are measured. This is done by replacing the flexible panel by a rigid panel equipped with an array of 30 flush-mounted 1/4" microphones, in a  $5 \times 6$  distribution, as illustrated previously in Figure 1 c). 200

Figure 3 illustrates the autopower spectra of the pressure fluctuations for the three considered grazing flow speeds, averaged over the 30 measurement points. Here, it is worth pointing out that as the flow speed changes, the flow temperature also changes. The average flow temperatures are  $32^{\circ}\text{C}$ ,  $36^{\circ}\text{C}$  and  $40^{\circ}\text{C}$  for  $U^{(1)} = 9 \text{ m/s}$ ,  $U^{(2)} = 14 \text{ m/s}$  and  $U^{(3)} = 19 \text{ m/s}$ , respectively. As can be seen, higher speeds cause higher pressure amplitudes, with higher flow energy at lower frequencies. Some sharp peaks can be noticed such as the ones at 470 Hz and 280 Hz for the  $U^{(1)}$  and  $U^{(2)}$  grazing flow cases, respectively, which are caused by the pressure pulsations at the outlet of the roots blower and determined by its rotational speed. 205

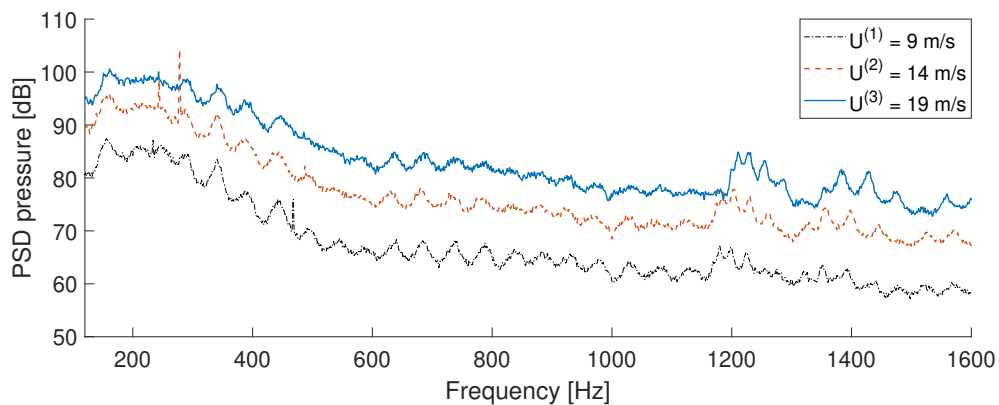


Figure 3: Averaged autopower pressure of the grazing flow pressure fluctuations with three different speeds  $U^{(1)} = 9 \text{ m/s}$ ,  $U^{(2)} = 14 \text{ m/s}$  and  $U^{(3)} = 19 \text{ m/s}$ . Reference pressure:  $20 \mu\text{Pa}$ . 210

### 2.1.2. Wake pressure fluctuations

In this work, the effect of a bluff object wake is explored by attaching cylinders [39–41] upstream the test section for a fixed flow speed  $U^{(3)} = 19$  m/s. Given the relatively high Reynolds number  $Re^{(3)} = 2.6 \cdot 10^6$  for the conditions in study, a regular von Karman street may no longer exist and a broadband pressure excitation can be achieved [14]. Moreover, for the calculated Reynolds numbers as a function of the bluff object diameters, a Strouhal number  $St \approx 0.2$  is obtained, as studied in [42]. The Strouhal number can be used to have an estimation at which frequency the vortices propagate and is typically defined as  $St = f D/U$ , where  $f$  is the frequency in Hz,  $D$  the cylinder diameter in m and  $U$  the flow speed in m/s. Thus, for each diameter considered, this corresponds to  $f_1 \approx 760$  Hz,  $f_2 \approx 633$  Hz and  $f_3 \approx 480$  Hz for  $D_1 = 5$  mm,  $D_2 = 6$  mm and  $D_3 = 8$  mm, respectively.

Figure 4 shows the averaged autopower spectra of the pressure fluctuations for the considered cases of excitation by the wake of bluff cylinders, comparing them with the pressure spectrum for a grazing flow with  $U^{(3)} = 19$  m/s. The figure shows that the addition of the cylinders upstream lead to zones of increased pressure levels that shift to lower frequencies as the diameter of the cylinders increases. A closer inspection of Figure 4 shows that two peaks are present for each case: (i) one near the predicted frequencies and (ii) another at a higher frequency. The two peaks occur due to the fact that the flow is turbulent and its speed inside the duct is not uniform [43]. To verify this, inspections of individual microphones in two different positions within the same direction are performed, as shown in Figure 5. As can be seen, microphones near the edges (microphones 6 and 11) have their peaks near the predicted frequency  $f_2 \approx 633$  Hz while microphones in the center (microphones 8 and 13) have a peak at 710 Hz. It is important to mention that microphones 6 and 8 have a higher peak amplitude with respect to microphones 11 and 13, respectively, which can be due to a reduction of vorticity as the vortices propagate along the duct. However, given that the cylinder diameter and  $St$  are fixed, it can indicate that the flow speed is non-uniform and varies within the test section.

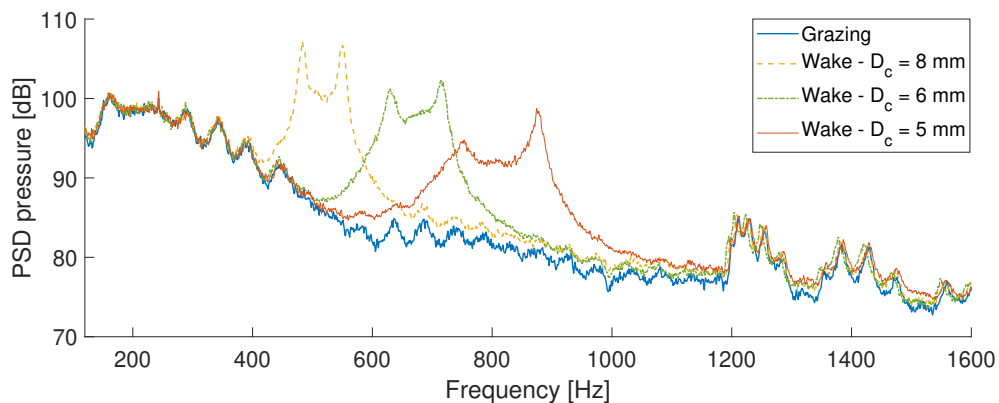


Figure 4: Averaged autopower pressure comparison for the three wake cases for  $U^{(3)} = 19$  m/s. Reference pressure:  $20 \mu\text{Pa}$ .

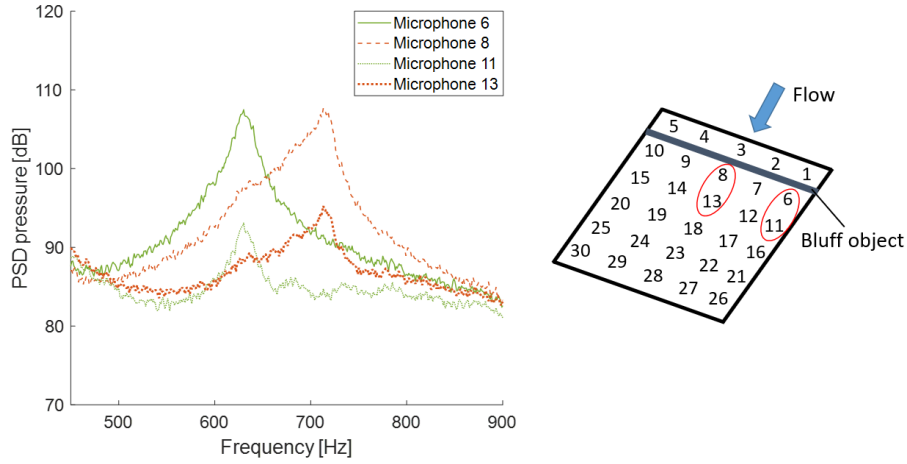


Figure 5: Individual measured autopower pressure for microphones at different positions in the array for  $U^{(3)} = 19$  m/s and bluff object with  $D_2 = 6$  mm attached upstream. The figure on the right shows a sketch of how the array of microphones is numbered. The two red circles highlight the microphones used in the verification. Reference pressure:  $20 \mu\text{Pa}$

## 2.2. Test plate

A steel flat plate with dimensions  $150 \times 200 \times 0.5$  mm is used as a host structure. 240  
This combination of material and dimensions is chosen such that a flexible structure with pronounced modal behavior in the low-frequency range below 1000 Hz is obtained. A modal analysis is performed on a free panel with dimensions  $350 \times 451 \times 0.5$  mm of the same material and model updating procedures are applied in order to retrieve the material properties, shown in Table 1. The flat plate is clamped by means of a frame and mounted flush 245  
as a side wall of a duct section, as shown in Figure 6.

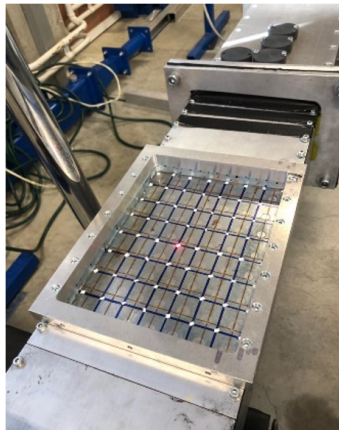


Figure 6: Illustration of the steel flat plate attached to the duct section.

Young's Modulus	Density	Poisson's Ratio	Structural Damping
233.1 GPa	7766.9 kg/m <sup>3</sup>	0.27	0.2%

Table 1: Material properties of the steel plate.

### 2.2.1. Grazing flow excitation

The dynamic behavior of the structure of interest is then evaluated with the presence of a grazing flow. The structural response of the flat plate is measured by a Scanning Laser Doppler Vibrometer (SLDV) over 72 points. Figure 7 compares the Root Mean Square (RMS) PSD autopower velocity response of the bare structure due to a TBL excitation for the three considered speeds. The figure shows that when excited by the TBL, the response of the plate is strongly dominated by structural modes below 1000 Hz while at frequencies above 1000 Hz, this behavior is less pronounced, with no clear peaks indicating structural modes, and the spectra seem dominated by the flow fluctuations, showing a similar behavior evidenced in Figure 3. However, between 1200 Hz and 1300 Hz, a possible mode may be excited e.g. 1230 Hz for the case of  $U^{(3)} = 19$  m/s, but since this frequency range is out of the scope of this paper, this is not further investigated.

The three spectra are similar in shape, however, some differences can be observed: (i) the vibration amplitudes are higher for the highest speed case, which is expected due to the fact that the excitation is also greater for a higher speed e.g. higher load levels, complying with Figure 3 and (ii) there is a trend of modes shifting to higher frequencies as the flow speed increases. The latter might be explained due to an increase of the flow temperature as the flow speed rises, as indicated in Section 2.1.1, which in turn increases the temperature of the material. This can introduce thermal effects to the structure such as thermal expansion. However, since the structure is clamped, it cannot move at its boundaries, which can lead to levels of pre-stress on the plate [44].

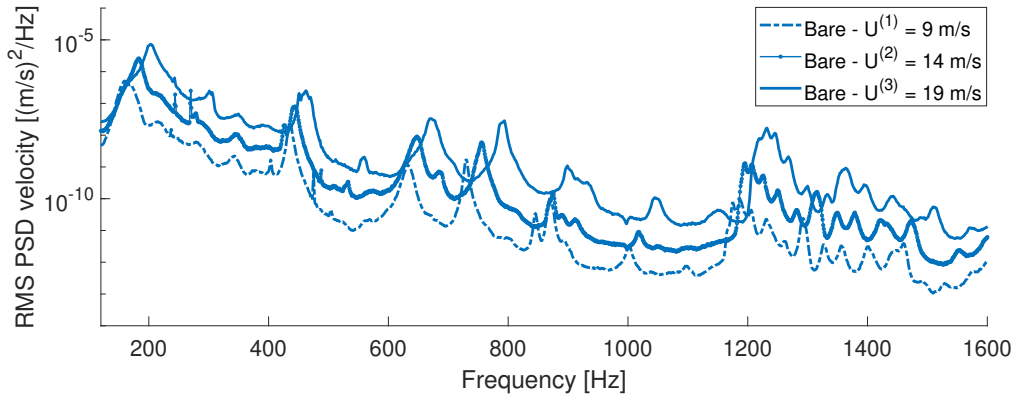


Figure 7: Comparison of experimental RMS PSD autopower velocity response of the bare flat plate for a grazing flow with different speeds of  $U^{(1)} = 9$  m/s,  $U^{(2)} = 14$  m/s and  $U^{(3)} = 19$  m/s.

In order to verify whether the temperature of the flow can indeed have an influence on the frequency of the modes, an investigation is performed by measuring via SLDV the

response of the plate at a fixed point in the center under the turbulent flow excitation for a constant speed, namely,  $U^{(3)} = 19$  m/s and with an increasing temperature, to assess the shift in frequency of the first mode of the plate. This evaluation is carried out within a period of time from when the roots blower is switched on, hence the flow starting at ambient temperature until the temperature of the flow is stabilized at 40°C. The frequency of the first mode is assessed over ten measurements, which are here referred to and numbered from T1 to T10, as shown in Figure 8. A representation of the first mode of plate is also illustrated and is derived from an FE model of the flat plate with the material properties shown in Table 1, by using the commercial FE software NX Nastran [45] and solved by SOL 103 Response Dynamics. The model consists of 3350 linear CQUAD4 shell elements and clamped boundary conditions.

Table 2 shows the shift in frequency of the first mode as the temperature of the flow changes. It can be seen that as the temperature of the flow varies from ambient until its stabilization point, the frequency of the first mode shifts to higher frequencies. It is important to mention that when the temperature of the flow stabilizes, the frequency of the mode stays constant. This can be an indication that the shift in frequencies of the modes can indeed be driven by the change in the flow temperature. The pre-stress levels related to each flow temperature are however not investigated since it is out of the scope of the paper.

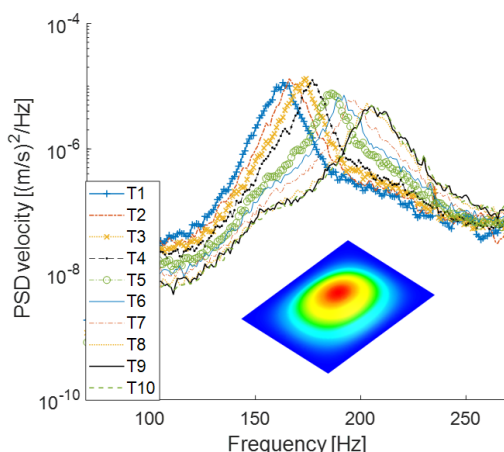


Figure 8: Comparison of experimental PSD autopower velocity response of the bare flat plate under a grazing flow excitation at different temperatures with  $U^{(3)} = 19$  m/s for the first mode.

Measurements	Frequency [Hz]	Temperature
T1	163	30°C
T2	166	31°C
T3	174	33°C
T4	177	34°C
T5	186	36°C
T6	192	37°C
T7	197	38°C
T8	203	40°C
T9	203	40°C
T10	203	40°C

Table 2: Frequency variation of the first mode as a function of the flow temperature for  $U^{(3)} = 19$  m/s.

In addition, as discussed in literature [46–49], the effect of aerodynamic damping can be expected with increasing flow speeds. In the work of Clark and Frampton (1997) [46], an investigation is performed on the effect of a subsonic flow over a non-lifting elastic plate. It is found that the dynamic behavior of the structure can be strongly modified as the flow speeds increase, which causes structural modes to shift to lower frequencies. This effect is more evident for the first mode of the plate, especially when Mach approaches 1.0, where a divergence occurs. In this regime, the frequency of the first mode significantly decreases and its peak highly reduced due an increase in the level of damping driven by the fluid-structure coupling [47]. Similar observations are evidenced by Vitiello et al. (2008) [48] and Ciappi et al. (2016) [49].

Nevertheless, closer inspections of Figure 7 show that the dynamic behavior of the plate does not exhibit the expected effects with increasing flow speeds. This is most likely explained by the Mach values considered in the present paper i.e.  $M^{(1)} = 0.027$ ,  $M^{(2)} = 0.041$  and  $M^{(3)} = 0.056$ , which are rather low to lead to perceptible effects since, as verified in [46], these are more noticeable for Mach values closer to 1.0. Furthermore, as discussed based on Figure 8, the shift in frequency of the modes can be reasoned to be driven by the temperature of the flow, which seems to be a more dominant factor in the case of this paper. However, albeit the flow speeds are relatively low, they can still be used as a representative excitation for the purpose of the paper, which is to demonstrate the potential of LRMs to reduce flow-induced noise and vibration at the lower frequency range below 1000 Hz.

### 2.2.2. Wake excitation

In order to perform the study for an excitation by the wake of a bluff object in the flow, the case when a bluff cylinder with  $D_c = 6$  mm for  $U^{(3)} = 19$  m/s is used here. Figure 9 shows the experimental bare plate response under grazing flow and turbulent wake excitation. At 570 Hz, an even mode exists in the panel (confirmed experimentally), which is not well excited by the grazing flow. However, when the structure is excited by the turbulent wake, this mode is amplified. A representation of the structural mode at 570 Hz is also shown in

Figure 9. This mode shape is derived from an FE model used for the mode shape in Figure 8. 315

Furthermore, albeit less pronounced, an amplified frequency region is noticed around 700 Hz. These results indicate that when a wake is generated by the bluff cylinder, due to coupling effects of fluid-structure interaction, the energy coming from the turbulent wake is transferred to the structure and even modes can again be well excited. This in turn could lead to noise radiation. The fact that two amplified regions are observed can be due to the creation of two turbulent peaks at different frequencies when the cylinder is added upstream. In this work, a first LRM solution will be designed to focus on the frequency range around 600 Hz to treat this amplified mode due to the turbulent wake. 320

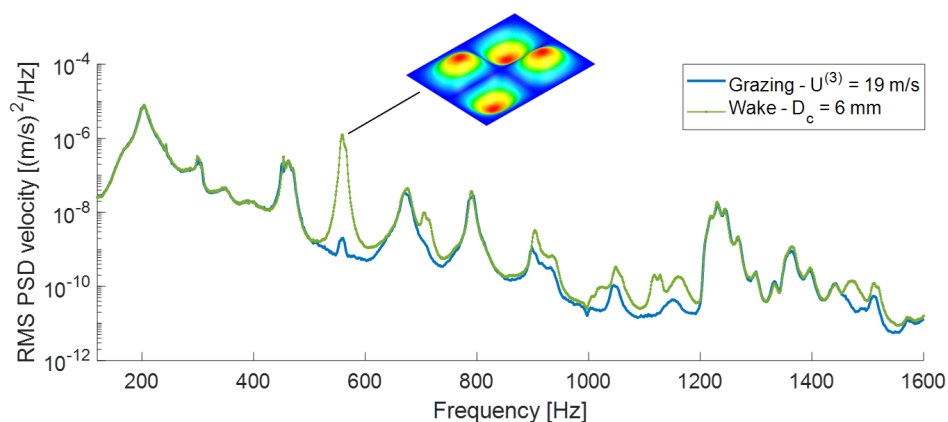


Figure 9: Comparison of RMS PSD autopower velocity of the bare flat plate under a grazing flow and flow with a cylinder of  $D_c = 6$  mm fixed upstream for  $U^{(3)} = 19$  m/s. 325

### 2.3. Backing cavity 330

To evaluate the sound radiated by the flow-excited steel panel and to investigate if LRMs can reduce noise radiation into confined spaces, a hard-walled backing cavity is placed over the flat plate set-up as shown in Figure 10 a), and the sound pressure levels (SPL) inside the cavity-backed plate are evaluated by means of one 1/4" microphone. The position of the flush mounted microphone is chosen as depicted in Figure 10 a). 335

The first acoustic mode of the cavity is predicted to be at 724 Hz with an out-of-plane direction with respect to the plate, as shown in Figure 10 b). This acoustic mode shape is calculated in NX Nastran and solved by SOL 103 Real Eigenvalues. The model consists of 32165 linear CTETRA4 - Acoustic fluid solid elements for air with same properties  $\rho_{air}$  and  $\mu_{air}$ , as indicated in Section 2.1 and  $c = 340$  m/s, where  $c$  is the speed of sound. Figure 11 illustrates the SPL inside the bare cavity-backed plate for a grazing flow of  $U^{(3)} = 19$  m/s, with the mode at 724 Hz highlighted. 340

In the next section, a second LRM solution will be designed for the plate to target the frequency region of this acoustic mode at 724 Hz, considering a TBL excitation, considered as a different frequency problem with respect to the wake excitation frequency range. 340

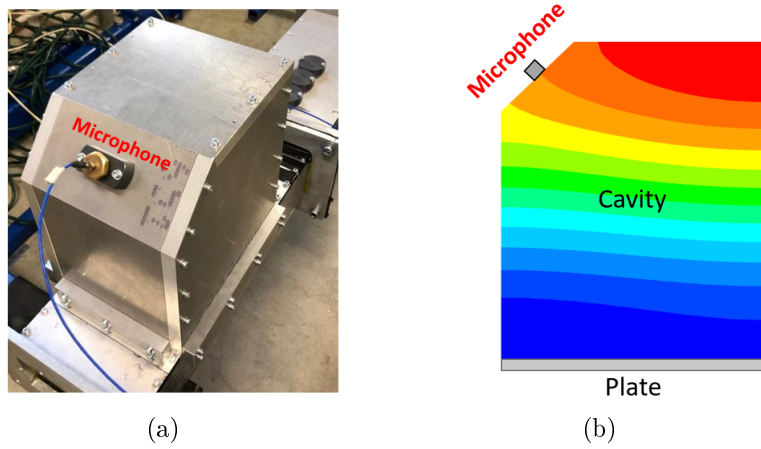


Figure 10: Illustration of the cavity-backed plate attached to the duct section a) Realized and b) Side view of the acoustic mode of the backing cavity at 724 Hz with an out-of-plane direction with respect to the plate, where the red and blue areas indicate points with the highest and lowest pressure values, respectively.

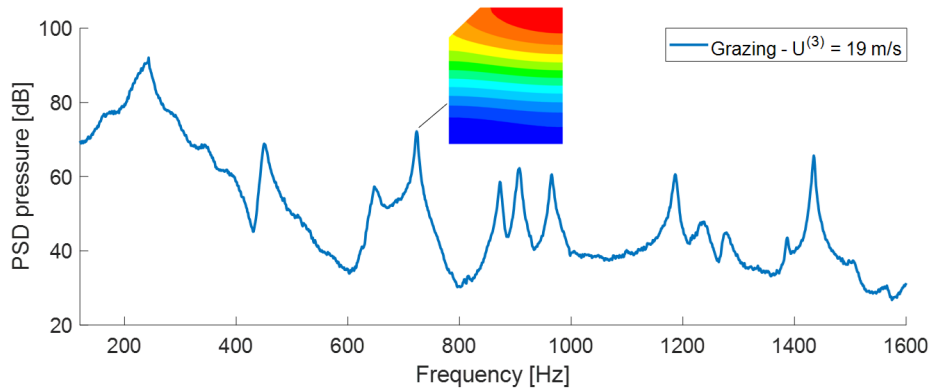


Figure 11: PSD autopower pressure response inside the bare cavity-backed plate under a grazing flow excitation for  $U^{(3)} = 19$  m/s. Reference pressure:  $20 \mu\text{Pa}$ .

With the goal to investigate the use of LRMs to reduce the noise radiated by the amplified vibrations of the flat plate due to the turbulent wake, the same cavity-backed plate setup is utilized. An evaluation of the SPL inside the cavity-backed plate is again performed and the case of a TBL excitation is used as a reference. Figure 12 illustrates the comparison of SPL inside the bare cavity-backed plate under TBL and turbulent wake excitation for  $U^{(3)} = 19$  m/s. The results indicate that the amplified structural mode leads to a higher overall SPL inside the cavity-backed plate around the frequency range of 600 Hz. In addition, a pressure amplification is perceived around 700 Hz, which can be due to the vibration amplification around such frequency band, as shown in Figure 9. The LRM solution to target the 600 Hz frequency range will then be used to evaluate the LRM performance to suppress the amplified noise radiation due to turbulent wake excitation.

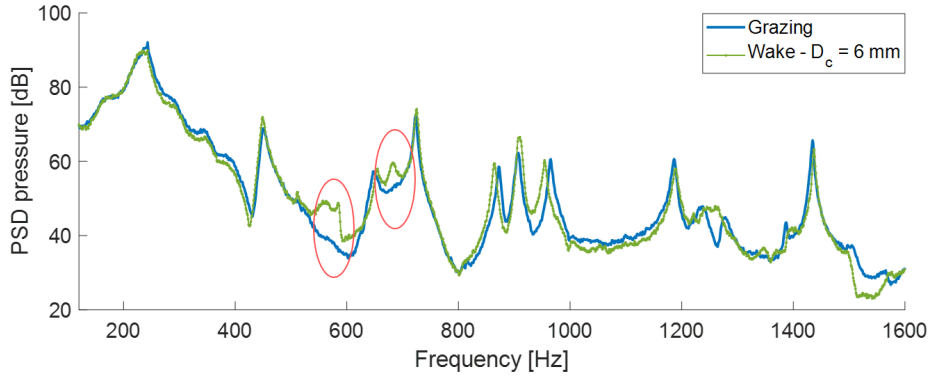


Figure 12: Comparison of PSD autopower pressure inside the bare cavity-backed plate under a grazing flow and flow with a cylinder of  $D_c = 6$  mm fixed upstream for  $U^{(3)} = 19$  m/s. The red circles highlight the frequency ranges where an amplification is observed. Reference pressure:  $20 \mu\text{Pa}$ .

### 3. LRM design

This section presents the LRMs design used to obtain stop bands to tackle the NVH behavior caused by aerodynamic excitation. Two LRM solutions are designed to tackle the frequency regions discussed in the previous section for a grazing flow and wake excitation. Additionally, the designed LRM solutions are combined in order to target two frequency bands simultaneously under the excitation of the wake of a cylinder in the flow.

#### 3.1. Resonator designs

This study considers two frequency ranges of interest for the steel plate, thus, two LRM solutions are proposed to tackle the frequency regions for the two flow excitation of the system: (i) design **A**, targeting the noise and vibration amplification around 600 Hz caused by the wake of the cylinder and (ii) design **B**, developed to tackle the TBL-induced vibration and noise radiation around the frequency range of the acoustic mode of a backing cavity at 724 Hz.

In this work, the design of the LRM solution takes into consideration the findings from the work of Claeys et al. (2013) [50]: (i) larger relative mass additions lead to wider stop bands for the same design frequency and (ii) for a same relative mass addition and same design frequency, if the spacing between resonators is small enough with respect to the structural wavelength of the targeted waves, the achieved global vibration reduction around the targeted frequency range saturates.

To develop the designs, case **B** is used as a reference, in which the goal is to design a LRM solution capable of creating a stop band wide enough to not only strongly reduce the vibrations around 724 Hz but also around the frequency region of the subsequent mode of the plate at higher frequencies. As shown in Figure 7, such mode varies in frequency according to the flow speed used: (i)  $f_{mode} = 730$  Hz for  $U^{(1)} = 9$  m/s, (ii)  $f_{mode} = 756$  Hz for  $U^{(2)} = 14$  m/s and (iii)  $f_{mode} = 789$  Hz for  $U^{(3)} = 19$  m/s. A shift in frequency of the mode for different flow speeds is expected, as explain in Section 2.2. This means that the designed solution needs to lead to a stop band at least 65 Hz wide to cover the frequency

range from 724 Hz until 789 Hz to assure the design goal. Design **A** is then derived from  
380 design **B**.

The resonator designs for each case are respectively illustrated in Figure 13 a) and d).  
A similar cantilever-beam resonator design with an end point mass has been investigated  
in [51]. The resonant additions are designed with similar modal effective mass [52] and tuned  
to the targeted frequency range through iterations on their dimensions. For each iteration,  
385 the resonance frequency of their first bending mode is evaluated by using a FE model  
and clamped base boundary conditions in NX Nastran and solved by SOL 103 Response  
Dynamics. The FE model for designs **A** and **B** consist of 504 and 520 linear CHEXA8 solid  
elements, respectively. All resonators are made of polymethyl methacrylate (PMMA) and  
are manufactured by means of laser-cutting. Therefore, during the iterations, the width  
390 of the resonators is kept fixed to 4 mm. The material properties of PMMA are shown in  
Table 3.

The two resonators are designed and realized such that they possess a similar mass,  
namely 0.59 g for design **A** and 0.55 g for design **B**. They both have a modal effective mass  
ratio i.e. ratio between their respective modal effective masses and nominal masses, around  
395 63%. The design approach also takes into account the footprint of the realizable resonators,  
since it is known that smaller footprints can lead to wider stop bands [53]. To be able to  
compare, in a later stage, the LRM reduction performance with an equivalent mass case,  
a block with its first resonance frequency at 5260 Hz, i.e. no resonant behavior within the  
targeted frequency range and with similar added mass as the resonators, namely, 0.57 g, is  
400 also designed and realized, as illustrated in Figures 13 g) and h), respectively. The difference  
in mass values between the resonant and non-resonant additions is deemed small and should  
not affect the conclusions significantly.

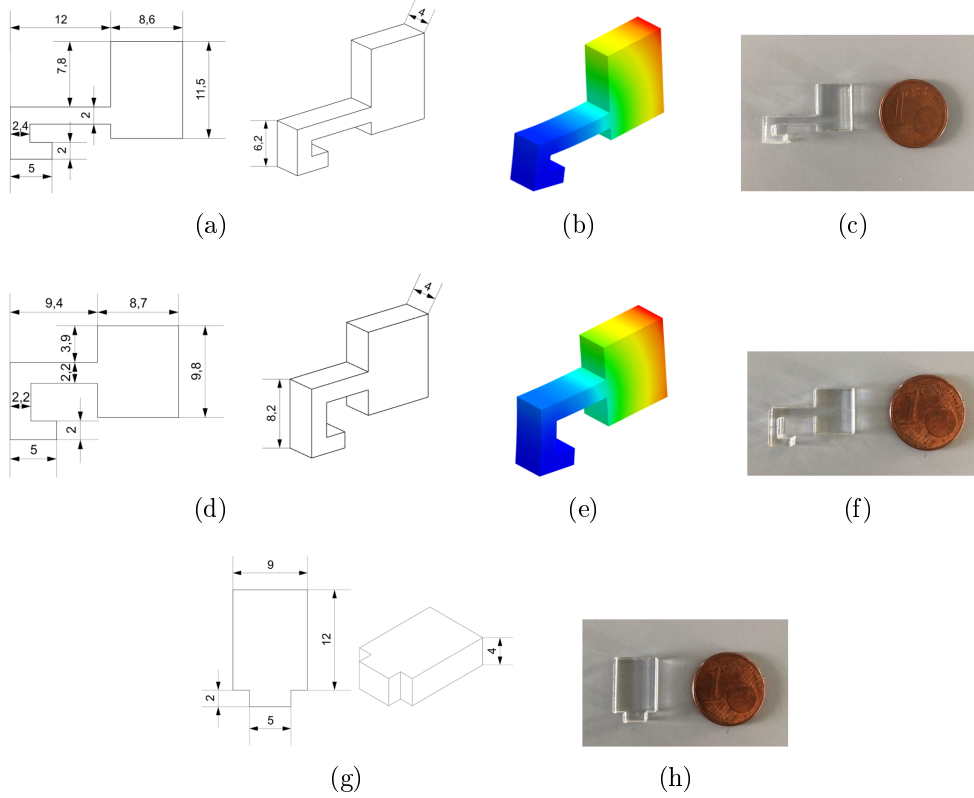


Figure 13: Illustration of a) resonator **A** design b) out-of-plane bending mode of resonator **A** c) realized resonator **A** d) resonator **B** design e) out-of-plane bending mode of resonator **B** f) realized resonator **B** g) non-resonant structure design and h) realized non-resonant structure.

Young's Modulus	Density	Poisson's Ratio	Structural Damping
4850 MPa	1188.38 kg/m <sup>3</sup>	0.31	5%

Table 3: Material properties of PMMA [51].

### 3.2. LRM configurations

The resonators are then added to the steel plate in a rectangular pattern with a spacing of  $21 \times 25$  mm in order to be on a subwavelength scale in the frequency ranges of interest and achieve the desired stop band behavior. A total of 56 resonators can be added to the steel host structure.

In total, six cases are considered in this work:

- Bare case (Bare): flat plate without resonant structures, used as a reference.
- Single resonator type (SRT-A) case: flat plate entirely covered with 56 added resonators of design **A** in a  $7 \times 8$  grid pattern of  $21 \times 25$  mm, which target flexural waves propagating around 600 Hz, as in Figure 14 a). In this case, the LRM solution

adds in total 29% of mass with respect to the mass of the bare plate. This configuration is used to reduce flow-induced noise and vibration for the plate in the wake of a bluff cylinder.

- Single resonator type (SRT-B) case: flat plate entirely covered with 56 added resonators of design **B** in a  $7 \times 8$  grid pattern of  $21 \times 25$  mm, which target flexural waves propagating around the frequency range of the acoustic-driven mode of the cavity-backed plate, as in Figure 14 b). In this case, the LRM solution adds in total 27% of mass with respect to the mass of the bare plate. This configuration is used to mitigate flow-induced noise and vibration of the plate under TBL excitation.
- Mixed case (Mixed): flat plate with 28 resonators of design **A** alternated with 28 resonators of design **B** mixed in a  $3 \times 4$  grids of  $42 \times 50$  mm, as shown in Figure 14 d). The total mass addition for this LRM configuration corresponds to approximately 28% with respect to the mass of the bare plate. This configuration is used to tackle two issues simultaneously.
- Single resonator type (Checkered-B) case: flat plate covered with 28 added resonators of design **B** on a checkered pattern, as in Figure 14 c). In this case, the considered spacing dimensions are adjusted such that a minimum grid size is achieved, since the spacing between each resonant addition is larger in this case, as shown in Figure 14 c). The LRM solution adds in total 13.5% of mass with respect to the mass of the bare plate. This configuration is used in order to check how the LRM reduction performance is affected by removing half of the resonant elements and also serves as a reference for the mixed case.
- Equivalent mass case (EQM): flat plate entirely covered with 56 non-resonant additions in a  $7 \times 8$  grid pattern of  $21 \times 25$  mm. For this case, the total mass addition is 28% with respect to the mass of the bare plate, as shown in Figure 14 e).

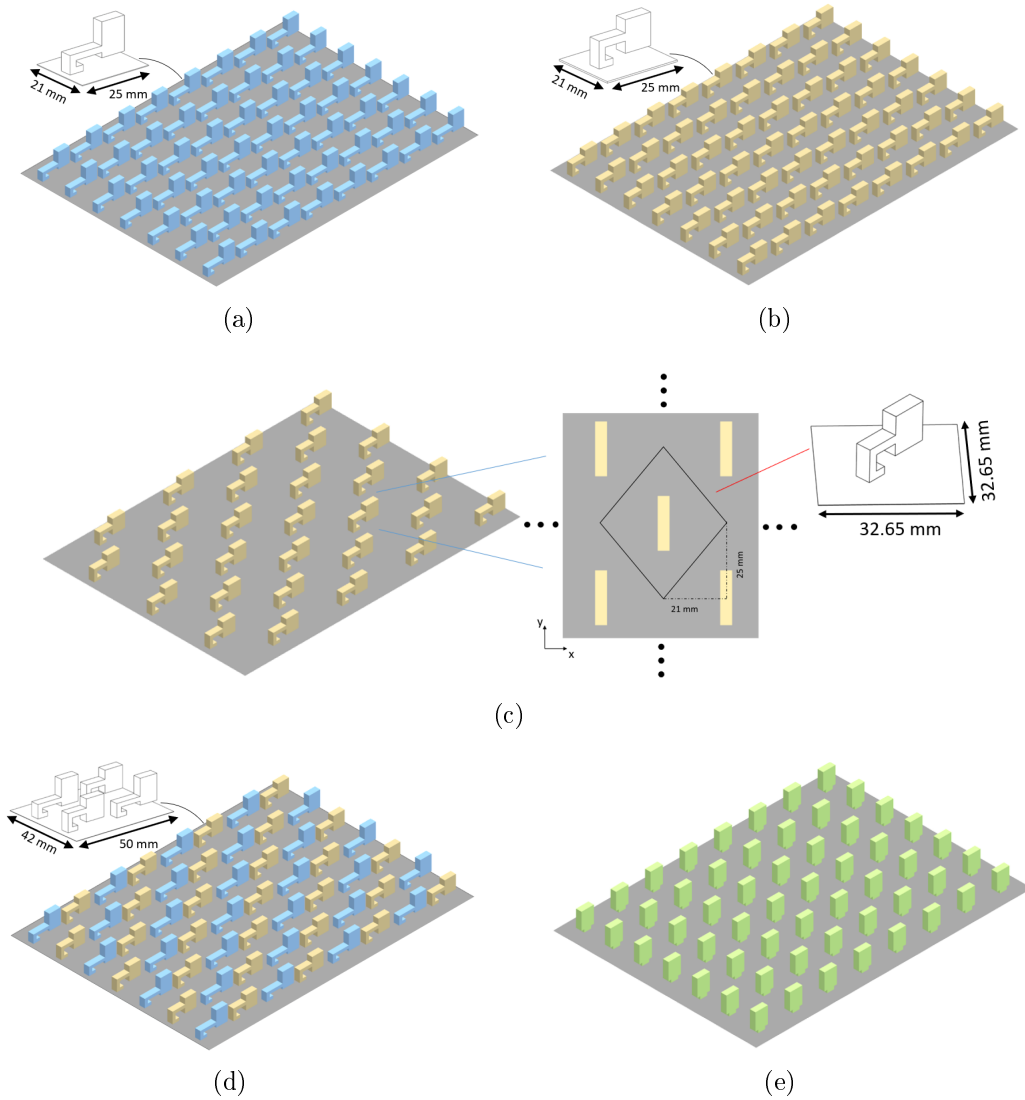


Figure 14: Illustration of LRM configurations a) SRT-A b) SRT-B c) Checkered-B d) Mixed and e) EQM.

### 3.3. Stop band limits

Given the typical periodic arrangement of LRMs, the stop band prediction can be carried out by unit cell (UC) modeling. Such modeling technique enables the calculation of the wave propagation in an infinite periodic structure based on the model of a single representative UC in combination with the Bloch-Floquet periodic boundary conditions. The present study assesses the wave propagation in an undamped infinite periodic structure by the computation of dispersion curves within the irreducible Brillouin contour (IBC). For more information on this modeling approach, the interested reader is referred to [24, 30, 50].

In order to have an indication of the relationship between the spacing among resonators and stop band widths for the configurations present in the paper, an investigation is performed for when resonators of design **B** are added to a host structure with material properties

	UC size [mm]	Mass addition	Stop band limits [Hz]	Stop band widths [Hz]
i)	$22 \times 22$	29%	769 - 845	76
ii)	$24 \times 24$	25%	764 - 835	71
iii)	$26 \times 26$	21%	758 - 825	67
iv)	$28 \times 28$	18%	753 - 816	63

Table 4: Summary of the relationship for the spacing between resonant additions and stop bands.

as in Table 1 in four different grid size configurations, as illustrated in Figure 15. The UC  
 450 lengths are varied in the x and y directions as the wave propagation is analyzed here for both  
 directions. It is worth mentioning that the subwavelength criterium is still respected in all  
 cases. The fact that the resonator design is kept the same while added in different patterns  
 leads to different relative mass additions. It is important to mention that if the goal was to  
 keep always the same relative mass addition, a different resonator design would have to be  
 455 made and tailored for each UC size. Hence, the approach of using only one design for the  
 investigation is chosen here.

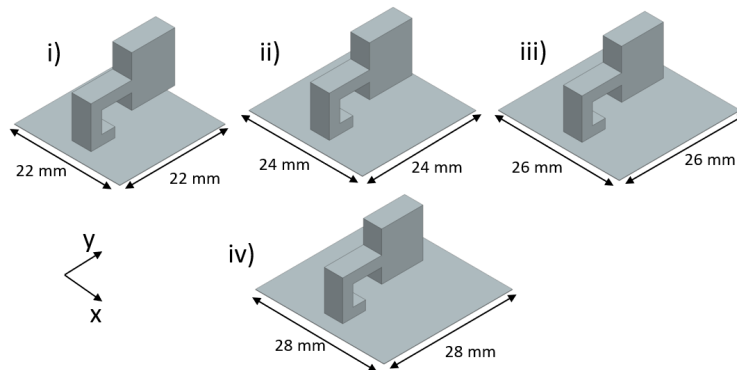


Figure 15: Overview of resonators of design **B** added to the host structure in different configurations.

Table 4 and Figure 16 illustrate the relationship between the spacing among resonators  
 and stop band widths. It can be seen that wider stop bands are obtained as the spacing  
 between resonators decreases. This is due to the fact that since the resonator design is kept  
 460 constant, the relative mass addition increases as the unit cell gets smaller, which complies  
 with the findings of Claeys et al. (2013) [50].

The predicted stop bands of the LRM designs SRT-A, SRT-B, Checkered-B and Mixed  
 are illustrated in Figure 17, and their stop band limits summarized in Table 5. It is worth  
 mentioning that the design goal for SRT-B is assured since its predicted stop band is 66.7 Hz  
 465 wide. In addition, the effects summarized in Table 4 can be translated to the predicted stop  
 bands for SRT-B as well as Checkered-B cases, which the former produces a wider stop band  
 than the latter, since the SRT-B configuration has a smaller spacing between resonators and,  
 consequently, a larger mass addition with respect to Checkered-B.

For the mixed configuration, two stop bands are predicted: one stop band opens from

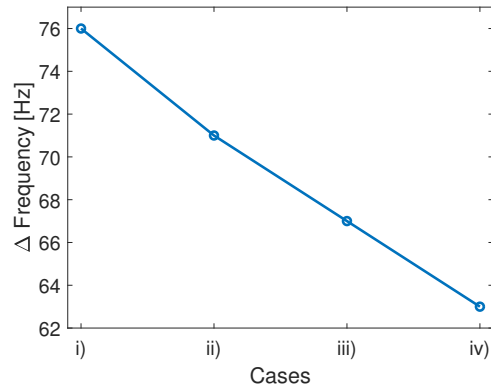


Figure 16: Illustration of the stop band widths of each configuration in Figure 15.

566.8 Hz to 605 Hz which is related to resonator design **A**, and another stop band is created 470  
 from 736.3 Hz to 800.2 Hz, which is related to resonator design **B**. These stop bands are  
 slightly narrower than the cases in which only one resonator type is added to the plate since  
 for each targeted frequency range only half of the resonators tuned to that specific frequency  
 is present within the same area.

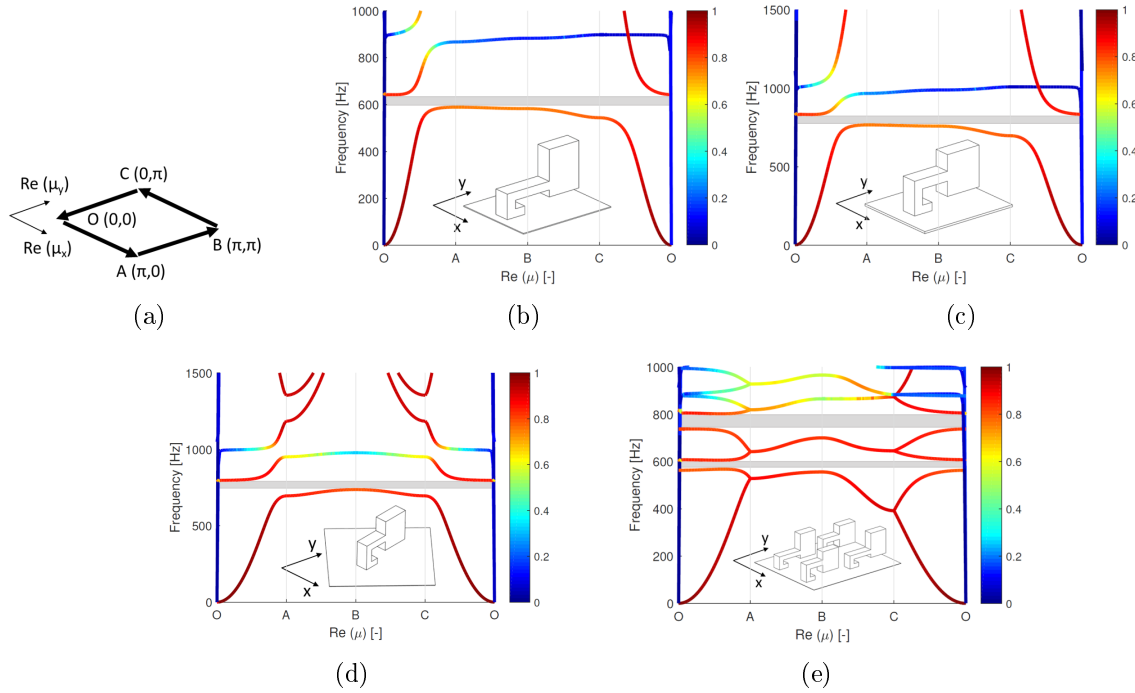


Figure 17: Representation of the a) Irreducible Brillouin Contour b) Dispersion diagram for SRT-A c) Dispersion diagram for SRT-B d) Dispersion diagram for Checkered pattern-B and e) Dispersion diagram for the Mixed case. The gray shaded area represents the predicted stop band for each configuration. The color bar illustrates the ratio according to the out-of-plane and in-plane motion of the waves, where 0 is total by in-plane and 1 total by out-of-plane.

Configuration	Resonator type	Stop band limits (Hz)
SRT-A	A	583.2 - 634.9
SRT-B	B	766.3 - 833
Checkered-B	B	736.7 - 801.3
Mixed	A & B	566.8 - 605 & 736.3 - 800.2

Table 5: Summary of the predicted stop bands for the LRM configurations.

#### 475 4. Experimental results

This section discusses the experimental results of the vibrations of the flat plate and their consequential noise radiation into a cavity-backed plate due to a turbulent flow excitation of the system. Firstly, the resonance frequency of the realized resonators is validated. Secondly, the use of LRMs to tackle a TBL excitation of the plate is investigated. An assessment is then performed on the LRM performance to reduce the noise radiation into the backing cavity. Subsequently, the designed LRM solution is assessed to reduce the amplified vibrations and

noise radiation occurring due to the turbulent wake excitation. Lastly, the designed LRM solutions are combined to tackle two NVH issues simultaneously.

#### 4.1. Validation of the resonator designs

In order to validate the resonance frequency of the resonators, the same methodology used in [51] is applied. Fifteen realized resonant addition samples of each type are glued to a metal block, rigidly connected to the stinger of a shaker, and the velocity at the tip of the resonator is measured by SLDV, such that the frequencies associated to the out-of-plane mode of the resonators can be identified. An average value of resonance frequency  $\bar{f}$  is calculated for each type of resonator by a linear average of the measured resonance frequencies. Table 6 shows the comparison between the numerical and experimental resonance frequencies for the two designs, which indicates that the values are relatively close to the design frequency with nearly the same standard deviation.

Resonator	Numerical (Hz)	Experimental (Hz)	% Standard Deviation
Type A	635	$641 \pm 7.88$	1.2
Type B	816	$819 \pm 9.05$	1.1

Table 6: Comparison between the simulated and measured resonance frequencies for resonators **A** and **B**.

#### 4.2. TBL-induced vibration of a flat plate

For the analysis, four cases are compared: (i) the bare plate, (ii) SRT-B, (iii) Checkered-B and (iv) EQM. Figure 18 a), b) and c) illustrate the response of the flat plate under grazing flow excitation with and without LRMs for  $U^{(1)} = 9$  m/s,  $U^{(2)} = 14$  m/s and  $U^{(3)} = 19$  m/s, respectively. For the SRT-B configuration, a pronounced zone of attenuation can be observed in the response of the plate around the predicted stop band, indicated by the black vertical lines. In fact, an improvement can be noticed starting from a frequency range around 600 Hz, which is explained by the interaction between resonators and host structure and also due to the effective dynamic mass of the resonators [54], which increases at frequencies before the stop band and reaches a maximum at its lower limit. The SRT-B leads to a stronger attenuation than the checkered-B configuration, since the former has more resonators, and consequently more added mass, targeting the investigated frequency range. A similar behavior has been noticed in [51]. In addition, the LRM configurations behave more favorably than the equivalent mass case for the tested conditions. The results also suggest that the LRM solution works for different flow conditions. As observed, the proposed solution creates a broad zone of attenuation in all three spectra, which suggests that LRMs can cope with the mild shift of resonance frequencies caused by a moderate variation of the flow speed.

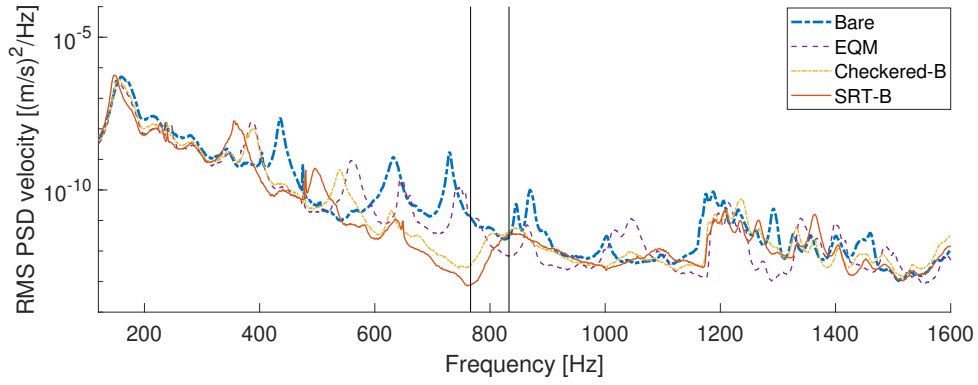
As discussed in the study of Claeys et al. (2013) [50], in a LRM solution, at frequencies slightly lower than the stop band region, an attenuation is achieved in the response of the finite structure, which indicates that the motion is localized in the tuned resonators and hence the structure itself has a lower response. While for frequencies slightly higher than the

stop band frequency range, the response of the structure is reinforced and the vibrational behavior of the plate is amplified. This effect is also evidenced in other works [55–58]. However, when increasing the damping present in the resonators, the zone of increased vibrational response after the stop band is attenuated, as also reported in [59–61]. In this present work, the designed LRM solution does not lead to any vibration amplification with respect to the bare structure at frequencies right after the upper limit of the stop band due to the damping present in the resonant additions. However, it can be seen in Figure 18 that there is some slight overshooting after the stop band region for the Checkered-B case with respect to SRT-B, which can be explained by the fact that less resonant additions are present in the Checkered-B case.

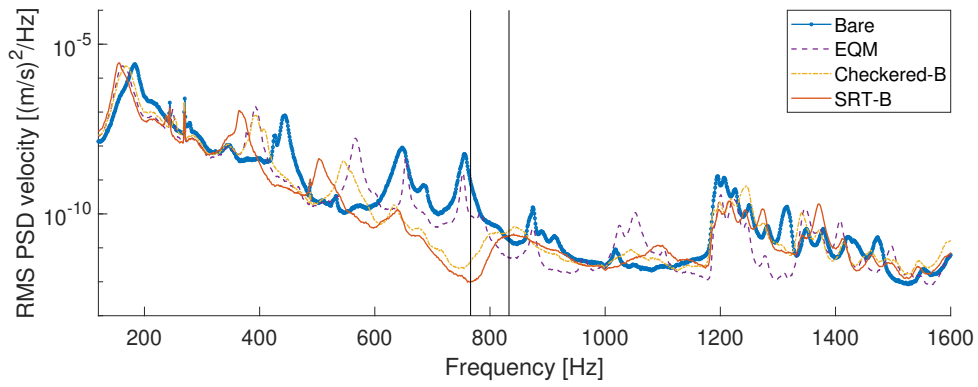
Even though the LRM solution leads to a strong vibration reduction at the targeted frequency for the three flow speed cases, it is worth identifying frequency ranges where the solution can lose performance with respect to its equivalent mass counterpart. To this end, the ratio between the amplitude vibration levels of EQM and SRT-B is computed and assessed for the frequency range within 120 Hz and 1600 Hz, for a fixed flow speed, namely,  $U^{(3)} = 19$  m/s. Figure 19 shows this relationship. For frequencies between 120 Hz and 550 Hz, the figure shows that zones of reduction and amplification alternate. These zones are driven by modal behavior and the overall vibration levels for SRT-B and EQM seem comparable in terms of peak amplitudes. From 550 Hz until the end of the stop band, the LRM solution shows a reduced vibration response compared to its equivalent mass counterpart. After the upper bound of the stop band, zones of vibration reduction and amplification again alternate. The appearance of the amplification zones after the stop band is typically linked to the behavior of the dynamic effective mass of LRMs, as studied in the works of Pai (2010) [62], Pai et al. (2014) [63] and de Melo Filho et al. (2019) [54].

As discussed by de Melo Filho et al. (2019) [54], at frequencies above the stop bands, albeit larger than for the bare case, the dynamic effective mass of a LRM structure is smaller than its equivalent static mass configuration. This means that the overall inertia of the SRT-B system can be lower at these frequencies and hence higher vibration levels for the same response can occur with respect to the EQM system. Nonetheless, due to the (limited) vibration of the resonant structure, the material damping in these structures is more effective as for the case of the equivalent masses, and hence a better damping of the vibration level is achieved. The interplay between these two effects explains why EQM seems to have a lower overall vibration baseline whereas SRT-B surpasses EQM at certain frequency regions, as evidenced in Figure 19. This behavior is expected for all following results in this study since the used stop band mechanism does not change in the present work.

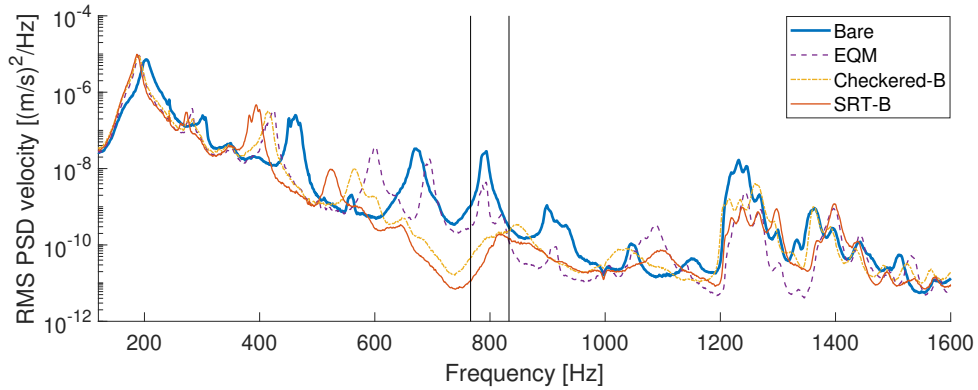
However, it is worth pointing out that when designing a LRM solution, the goal is to target a limited frequency region, as in the case of a tonal noise. If an improvement in the reduction performance of LRMs after the stop band frequencies is required, the LRM solution can be combined with classical solutions such as visco-elastic and constrained layers [64], which are performant at the high frequency range above 1000 Hz. However, since the goal of the paper is to only show the potential of LRMs to reduce flow-induced noise and vibration in the lower frequency range below 1000 Hz, this approach is not considered here.



(a)



(b)



(c)

Figure 18: Measured RMS PSD autopower velocity response of the flat plate with and without LRMs for a grazing flow with a)  $U^{(1)} = 9$  m/s b)  $U^{(2)} = 14$  m/s and c)  $U^{(3)} = 19$  m/s.

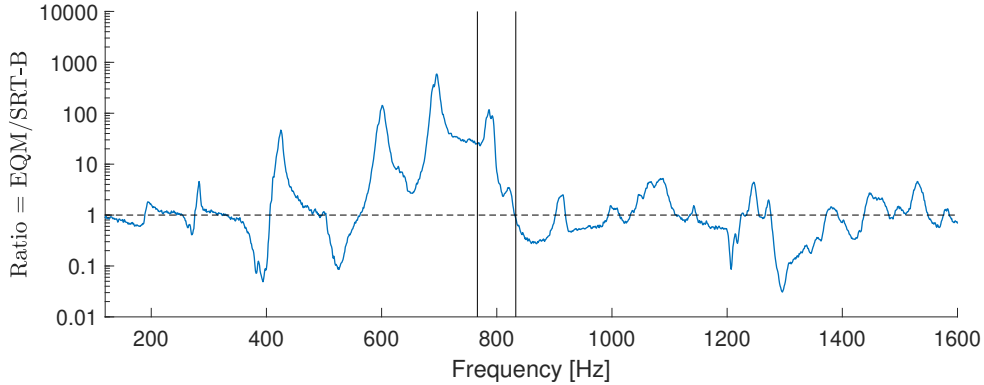


Figure 19: Ratio of the measured RMS PSD autopower velocity response of the flat plate between EQM and SRT-B for  $U^{(3)} = 19$  m/s, illustrated in logarithmic scale. The black dashed horizontal line at Ratio = 1 is used as reference. The area above this line indicates frequencies in which EQM has higher amplitude levels while the area below it represents frequencies where SRT-B possesses higher amplitude values. The two solid vertical lines represent the predicted stop band limits for the SRT-B configuration.

Furthermore, an investigation is carried out to have an indication of how the tested LRM configurations modify the original dynamic behavior of the plate by an experimental analysis of the vibration patterns of the structure below 1000 Hz, since the paper proposes to study the use of LRMs below this frequency. This investigation is here only carried out for the results related to a grazing flow excitation of the flat plate, shown in Figure 18. As indicated by Claeys et al. (2014) [65], the modal behavior in a LRM panel is drastically changed with respect to the bare panel or the EQM panel. Instead of the regular dispersion surface for bending waves, the addition of resonant elements leads to an in-plane dispersion surface before the stop band, no dispersion surface in the stop band frequency region and an out-of-plane dispersion surface after the stop band. Since the frequency of modes is related to the dispersion surfaces, as investigated by Mead and Parthan (1979) [66], this typically results in higher order modes with resonant elements moving in-phase being lowered in frequency and occurring before the stop band and typically lower order modes, with resonators moving out-of-phase, being repeated after the stop band. By comparing the first three modes of the bare panel, the EQM panel and the SRT-B panel, together with the first mode of the SRT-B panel after the stop band, this effect can be demonstrated. For the sake of simplicity, these mode shapes are verified for one flow speed, namely,  $U^{(3)} = 19$  m/s, since for other flow speeds, similar conclusions should hold, as only the excitation changes.

To investigate the modal behavior, operational velocities obtained via SLDV are used. At peaks in the frequency spectrum, the amplitude velocities of the scanned measurement grid are shown. Since these are operational velocity patterns, the resulting pattern is not the pure mode shape, but is the result of the forced response of the panel and its modal behavior, due to the turbulent boundary layer excitation. Figure 20 a) highlights the RMS PSD autopower velocity response of the plate up to 1000 Hz whereas Figure 20 b) illustrates the vibrational motion of the plate as well as the respective frequencies of the peaks for the considered resonant and non-resonant configurations. Three peaks are identified as modes of

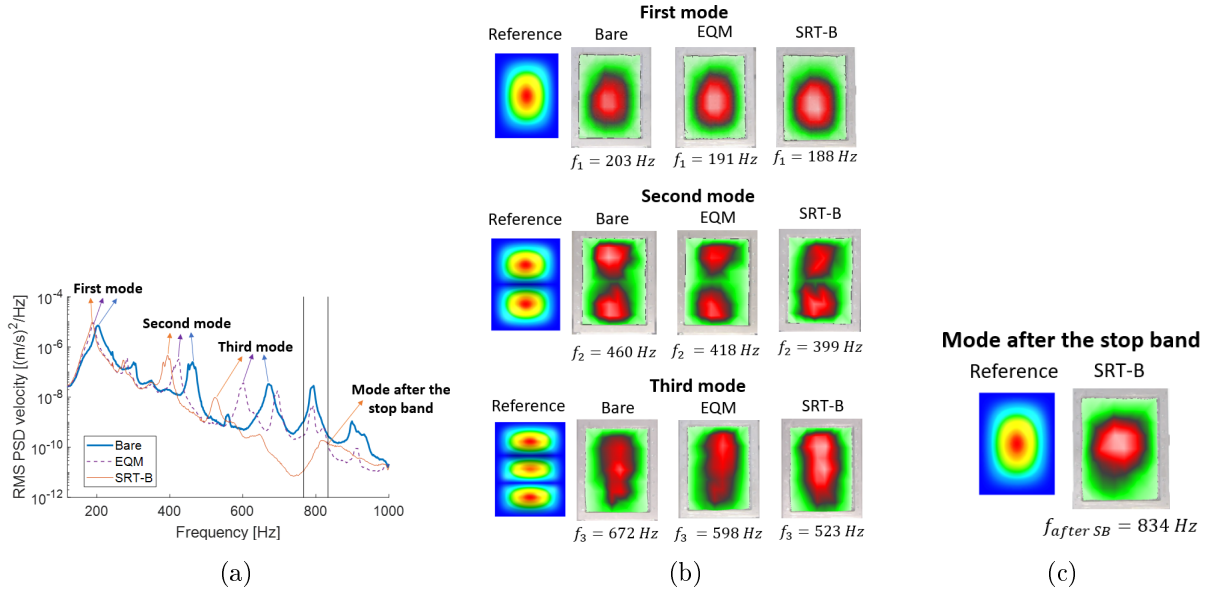


Figure 20: Illustration of the a) RMS PSD autopower velocity response of the structure for EQM and SRT-B configurations with  $U^{(3)} = 19 \text{ m/s}$  and b) vibration patterns of the first three peaks in the spectra for each configuration and c) vibration pattern of the first mode after the stop band (SB) for SRT-B. The red and green areas represent points of large and small motion of the plate, respectively.

a clamped plate, given that these have similar mode patterns as the modes obtained from the FE reference model of the clamped structure utilized earlier, for example, in Figure 8. This investigation confirms that when the resonators or mass blocks are added to the plate, the first modes are shifted to a lower frequency. It can also be seen that the shift in frequency is larger for the SRT-B panel and becomes larger as the modes come closer to the stop band frequency. This latter effect is caused by the dynamic mass of the resonant element becoming larger than the static mass when moving closer to the resonance frequency. The latter also explains why the amplitude of the third mode for panel SRT-B is lower than that of the bare panel or the EQM panel.

Figure 20 c) illustrates the vibration pattern of the first mode after the stop band for the SRT-B configuration, which shows a similar vibration pattern as for the first mode of the plate. This is in line with the work of Claeys et al. (2014) [65], which indicates that after the stop band, the mode shapes of the bare structure are repeated with the resonant elements moving out-of-phase with respect to the plate.

#### 4.3. Grazing flow-induced noise radiation into a cavity-backed plate

The same analysis as in previous section is repeated with an added backing cavity in order to evaluate the radiated noise. For brevity, the Checkered-B configuration is omitted.

Figures 21 a) to c) show the SPL inside the cavity-backed plate for the three considered cases and flow speeds. The black vertical solid lines represent the predicted stop band limits. In the spectra, different mode types can be seen: structural-driven and acoustic-driven modes. The former are the ones which vary with added mass due to the additions.

The latter are the ones for which no shift in frequency is perceived such as the modes at 724 Hz and 900 Hz. Before the predicted stop band, a relatively broad band of attenuation is obtained ( $\approx 500$  Hz - 750 Hz), which might be related to the reduction of the vibrations of the plate that begin even before the stop band due to the dynamic effective mass, as mentioned  
610 before. Inside the stop band limits, a sharp reduction zone can be seen in the three spectra close to the lower limit of the predicted stop band. After this zone of attenuation, the curves go up until the second acoustic driven mode of the coupled system around 900 Hz. It is also important to note that in all spectra, two structural-driven modes after the predicted stop band between 766.3 Hz and 833 Hz are no longer excited. This can be explained by  
615 the presence of damping in the resonators which is especially affecting the host structure after the stop band since the resonators are then still moving out-of-phase with respect to the host structure [50].

The figures show that the addition of resonators yields a peak-to-peak sound pressure reduction of around 20 dB, 22 dB and 21 dB at the first acoustic-driven resonance for the  
620 cases when  $U^{(1)} = 9$  m/s,  $U^{(2)} = 14$  m/s and  $U^{(3)} = 19$  m/s, respectively. The similar noise attenuation for all cases suggests that the flow speed barely affects the LRM performance. Furthermore, the LRM solution provides, in average, an additional 20 dB peak-to-peak noise reduction when compared to the equivalent mass case.

#### 4.4. Wake-induced vibration of a flat plate

As discussed in Section 2.2, the addition of the cylinder with  $D_c = 6$  mm fixed upstream the flat plate leads to a turbulent wake, which in turn can increase the excitation of specific structural modes. The SRT-A configuration is designed to suppress the vibrations of the flat plate around the frequency range where the highest pressure loads are expected for this configuration. Figure 22 compares the resulting vibrational response of the flat plate with  
630 and without LRMs for  $U^{(3)} = 19$  m/s. For the LRM configuration, a strong reduction zone can be observed in the spectrum around the predicted stop bands. In fact, an improvement can be noticed starting from the frequency range around 400 Hz. Furthermore, the designed metamaterial solution leads to a strong reduction around the the frequency range of the amplified mode of the plate.

In addition, the LRM solution outperforms the equivalent mass case for the tested conditions. It is important to note in the spectrum that the effect of adding the resonators can also be observed at higher frequencies. After the predicted stop bands, the overall amplitudes of the spectrum have decreased, which can be attributed to the damping in the resonators, as discussed in Section 4.3. The shift in resonance frequencies due to mass addition for the first  
640 modes of the plate can also be noticed in the spectra, for which similar vibration patterns are expected, as studied in Section 4.2.

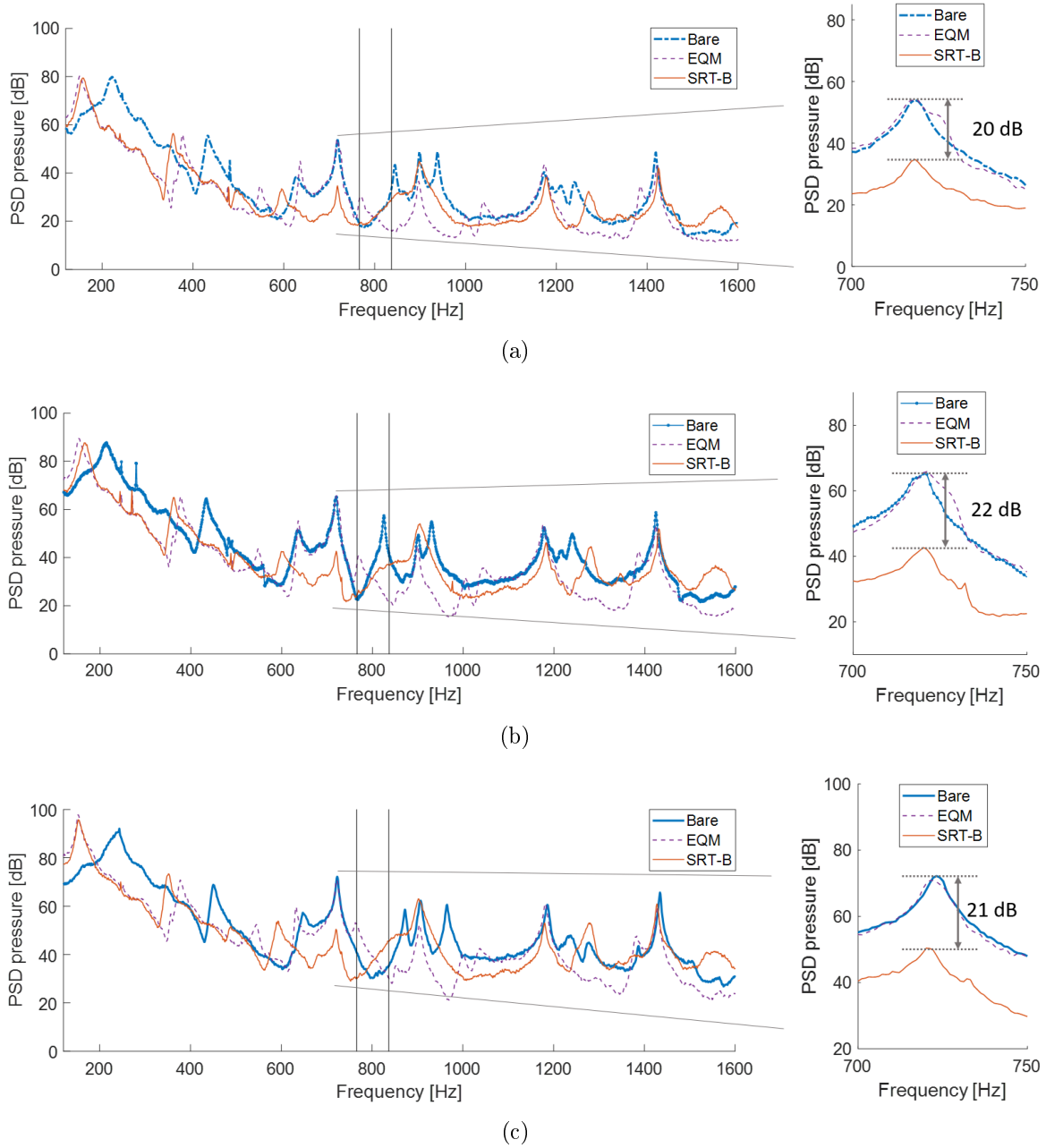


Figure 21: Experimental PSD autopower pressure response inside the cavity-backed panel with and without LRMs for a grazing flow with a)  $U^{(1)} = 9$  m/s b)  $U^{(2)} = 14$  m/s and c)  $U^{(3)} = 19$  m/s. Reference pressure:  $20 \mu\text{Pa}$ .

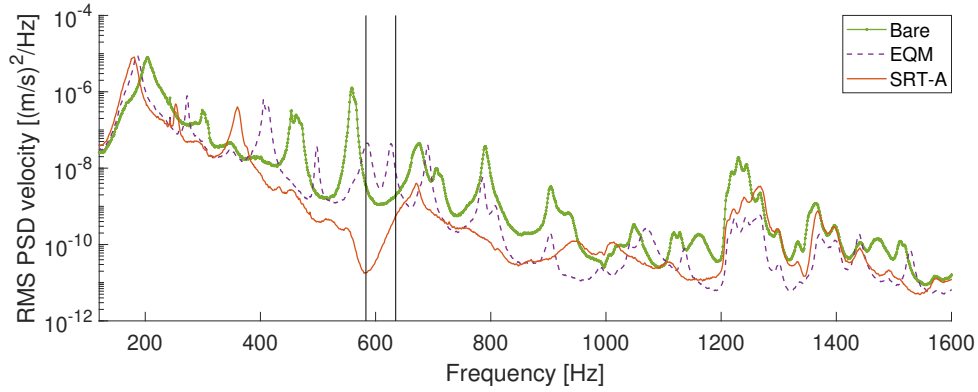


Figure 22: Measured RMS PSD autopower velocity response of the flat plate with and without LRMs for when a cylinder of  $D_c = 6$  mm is fixed upstream. The stop band limits are indicated by the solid black vertical lines.

#### 4.5. Wake-induced noise radiation into a cavity-backed plate

645 Figures 23 shows the comparison of the SPL measured inside the cavity for a plate with and without LRMs excited by the wake of a cylindrical rod. A pronounced zone of attenuation is noticed around the predicted stop bands. The figure at the right-hand side shows the pressure difference for each case within a frequency range  $\pm 30$  Hz with respect to the lower limit of the predicted stop band for the SRT-A configuration. The curves are obtained as the difference between the pressure levels of the bare case and each respective case for the considered frequency range. As can be seen, a maximum noise radiation reduction of 18 dB is achieved at 584 Hz. Furthermore, the LRM solution outperforms the equivalent mass case. In this case, even though the targeted frequency range is around 600 Hz, a 4 dB and 9 dB reduction can be noticed at the first (724 Hz) and second (910 Hz) acoustic driven modes of the cavity-backed plate, respectively, which may be due to the fact that the vibrational levels at these frequencies are reduced, as shown in Figure 22.

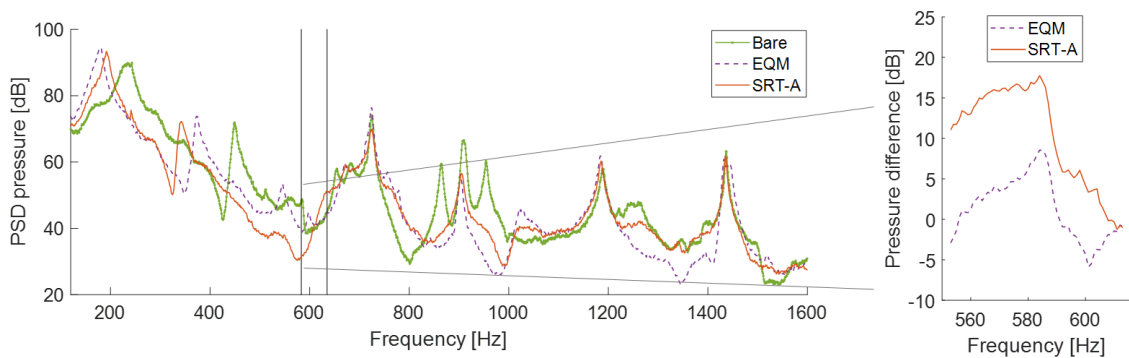


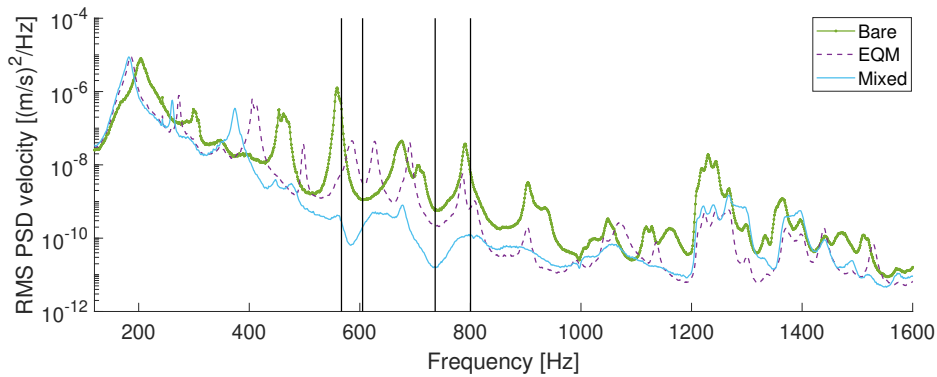
Figure 23: Experimental PSD autopower pressure response of the cavity-backed plate with and without LRMs for when a cylinder of  $D_c = 6$  mm is fixed upstream. The solid black vertical lines represent the previously predicted stop band limits. Reference pressure:  $20 \mu\text{Pa}$ .

#### 4.6. Tackling two frequency bands simultaneously

655

As a next step, it is investigated whether both LRM solutions, SRT-A and SRT-B, can be mixed to tackle two frequency ranges simultaneously in a combined approach, earlier defined as the Mixed case. The vibrations of the flat plate as well as the noise radiation into the cavity-backed plate are again measured and analyzed. For this analysis, the Checkered-B configuration is not considered for brevity and also due to its total added mass is half the Mixed configuration. 660

Figure 24 shows the responses for the bare and the LRM configuration when the cylinder of  $D_c = 6$  mm is placed upstream. For the mixed configuration, where the structure is treated with two types of resonators, two zones of attenuation are found: (i) one around 600 Hz related to the added resonators with design **A** and (ii) another zone around 730 Hz, related to the added resonators with design **B**. In the former zone of attenuation, the reduction is less pronounced than for the case when the entire plate is treated with the same type of resonator since less resonators that are targeting the same frequency are added. A similar trend is perceived as previously for the first modes of the plate, which are shifted to lower frequencies due to the mass addition. 665



670

Figure 24: Experimental RMS PSD autopower velocity response of the flat plate with and without LRMs for when a cylinder of  $D_c = 6$  mm is fixed upstream. The stop band limits for the mixed case are indicated with the solid black vertical lines.

An analysis of the noise radiation into the cavity-backed plate is also performed for the mixed LRM configuration, as shown in Figure 25. The same affected frequency regions are noticed: (i) the region of the amplified mode due to the interaction of the wake with the plate and (ii) the region of the first acoustic-driven mode of the cavity-backed plate.

For the former, the same pressure difference approach in section 4.5 is used, for a same frequency range. It can be seen that a maximum of 13 dB noise radiation reduction is obtained at 584 Hz, which is 5 dB less than the case when the entire plate is treated, as explained earlier. In the latter, a 9 dB peak-to-peak reduction is obtained at the frequency of the first acoustic driven mode of the system, which is an additional 5 dB reduction when compared to the case in Figure 23, for which a small reduction was obtained, possibly due to the damping in the resonators. Besides, the mixed LRM configuration also outperforms the 675

680

equivalent mass case. These results are an indication that a combined pattern of resonators is eligible to tackle flow-induced NVH issues of systems, where multiple frequency ranges are of interest.

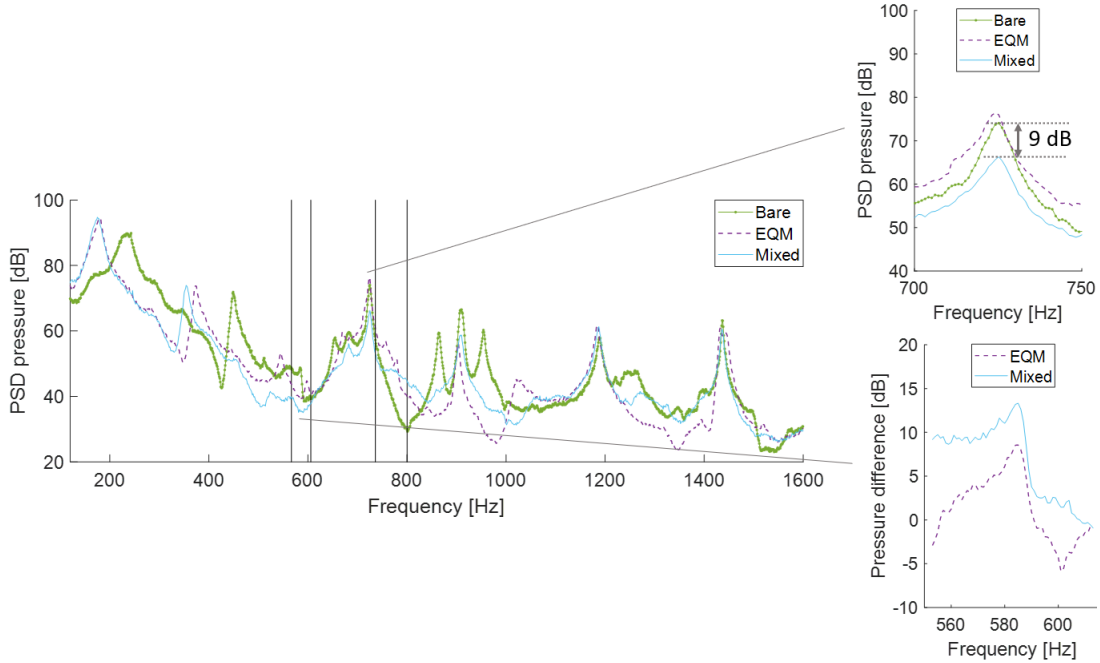


Figure 25: Experimental PSD autopower pressure response of the cavity-backed plate with and without LRMs for when a cylinder of  $D_c = 6$  mm is fixed upstream. The stop band limits for the mixed case are indicated with the solid black vertical lines. Reference pressure:  $20 \mu\text{Pa}$ .

## 685 5. Conclusion

This work presented an experimental investigation on the potential of using LRMs to suppress flow-induced noise and vibration of a plate. Two different aerodynamic loads are used, namely, a grazing flow and the wake of a bluff object.

690 Firstly, the flat plate vibrations under a grazing flow excitation are measured considering the bare plate, the plate treated with different LRM configurations and the plate with equivalent mass non-resonant additions. It is shown that LRMs provide a strong reduction of the vibrations of the plate in the targeted frequency range. The proposed solution is shown to outperform the equivalent mass case and to work for different flow conditions. The analysis of the cavity-backed plate system allows to evaluate the LRM potential to 695 reduce the noise radiation caused by the flow-excited vibration of the plate. The SPL inside the cavity-backed plate is measured and the results show that the LRM solution is also able to reduce the noise radiation at the first acoustic-driven resonance by approximately 20 dB.

700 Secondly, a LRM solution is designed to treat the same cavity-backed plate system excited by the wake of a bluff obstacle. It is shown that the addition of a bluff cylinder in the flow upstream to the plate leads to an amplification of a structural mode with respect to the

results for a grazing flow. Subsequently, a LRM solution is applied, targeting the frequency region where the largest amplification of vibrations is observed. It is shown that the LRM solution provides a strong reduction of the vibrations of the plate in the desired frequency range, leading to a maximum reduction of 18 dB of the noise radiated into the cavity-backed plate due to the amplified mode. The proposed solution also outperforms the equivalent mass case. 705

Lastly, the use of LRMs with multiple stop band behavior to tackle two frequency ranges simultaneously is investigated. It is shown that the Mixed LRM configuration creates two vibration reduction zones, albeit less pronounced than the cases in which the entire plate is treated with the same type of resonators. In addition, the creation of multiple stop bands not only suppresses the amplification of the radiated noise but also achieves a reasonable reduction in the first acoustic-driven mode of the system. 710

## 6. Acknowledgments

The research of F. A. Pires is funded by an Early Stage Researcher grant within the European Project SMARTANSWER Marie Curie Initial Training Network (GA 722401). This research was partially supported by Flanders Make, the strategic research centre for the manufacturing industry. The Research Fund KU Leuven is gratefully acknowledged for its support. 715

## References

- [1] J. Wilby, F. Gloyna, Vibration measurements of an airplane fuselage structure i. turbulent boundary layer excitation, *J. Sound Vib.* 23 (4) (1972) 443–466. doi:[https://doi.org/10.1016/0022-460X\(72\)90503-2](https://doi.org/10.1016/0022-460X(72)90503-2). 720
- [2] M. Howe, P. Shah, Influence of mean flow on boundary layer generated interior noise, *J. Acoust. Soc. Am.* 99 (6) (1996) 3401–3411. doi:<https://doi.org/10.1121/1.414988>.
- [3] B. Liu, H. Zhang, Z. Qian, D. Chang, Q. Yan, W. Huang, Influence of stiffeners on plate vibration and radiated noise excited by turbulent boundary layers, *Appl. Acoust.* 80 (2014) 28–35. doi:<https://doi.org/10.1016/j.apacoust.2014.01.007>. 725
- [4] C. Maury, P. Gardonio, S. Elliott, A wavenumber approach to modelling the response of a randomly excited panel, part ii: Application to aircraft panels excited by a turbulent boundary layer, *J. Sound Vib.* 252 (1) (2002) 115–139. doi:<https://doi.org/10.1006/jsvi.2001.4029>. 730
- [5] W. K. Blake, *Mechanics of flow-induced sound and vibration*. volume 1 general concepts and elementary source. volume 2-complex flow-structure interactions, *Appl. Math. Mech.* 1 (1986).
- [6] W. A. Strawderman, R. S. Brand, Turbulent-flow-excited vibration of a simply supported, rectangular flat plate, *J. Acoust. Soc. Am.* 45 (1) (1969) 177–192. doi:<https://doi.org/10.1121/1.1911353>.
- [7] A. Klabas, S. Callsen, M. Herr, C. Appel, Fuselage excitation during cruise flight conditions: from flight test to numerical prediction, in: *International Conference on Flow Induced Noise and Vibration Issues and Aspects*, State College, USA, Springer, 2017, pp. 309–324. doi:[https://doi.org/10.1007/978-3-319-76780-2\\_19](https://doi.org/10.1007/978-3-319-76780-2_19). 735
- [8] A. Caiazzo, W. Desmet, et al., A generalized corcos model for modelling turbulent boundary layer wall pressure fluctuations, *J. Sound Vib.* 372 (2016) 192–210. doi:<https://doi.org/10.1016/j.jsv.2016.02.036>. 740

- [9] C. Marchetto, L. Maxit, O. Robin, A. Berry, Measurement techniques of the sensitivity functions to characterize the vibration response of panels under turbulent boundary layer excitation, in: International Conference on Flow Induced Noise and Vibration Issues and Aspects, State College, USA, Springer, 2017, pp. 339–355. doi:[https://doi.org/10.1007/978-3-319-76780-2\\_21](https://doi.org/10.1007/978-3-319-76780-2_21).
- 745 [10] M. N. Ichchou, O. Bareille, B. Troclet, B. Hiverniau, M. D. Rochambeau, D. Chronopoulos, Vibroacoustics under aerodynamic excitations, in: Flinovia-Flow Induced Noise and Vibration Issues and Aspects, Springer, 2015, pp. 227–247. doi:[https://doi.org/10.1007/978-3-319-09713-8\\_11](https://doi.org/10.1007/978-3-319-09713-8_11).
- [11] T. Nakamura, S. Kaneko, F. Inada, M. Kato, K. Ishihara, T. Nishihara, N. W. Mureithi, M. A. Langthjem, Flow-induced vibrations: classifications and lessons from practical experiences, Elsevier, Amsterdam, 2013.
- 750 [12] J. Gerrard, The mechanics of the formation region of vortices behind bluff bodies, *J. Fluid Mech.* 25 (2) (1966) 401–413. doi:<https://doi.org/10.1017/S0022112066001721>.
- [13] Y. Lau, R. So, R. Leung, Flow-induced vibration of elastic slender structures in a cylinder wake, *J. Fluids Struct.* 19 (8) (2004) 1061–1083. doi:<https://doi.org/10.1016/j.jfluidstructs.2004.06.007>.
- 755 [14] M. Belloli, S. Giappino, S. Morganti, S. Muggiasca, A. Zasso, Vortex induced vibrations at high reynolds numbers on circular cylinders, *Ocean Eng.* 94 (2015) 140–154. doi:<https://doi.org/10.1016/j.oceaneng.2014.11.017>.
- 760 [15] W. Graham, Boundary layer induced noise in aircraft, part i: The flat plate model, *J. Sound Vib.* 192 (1) (1996) 101–120. doi:<https://doi.org/10.1006/jsvi.1996.0178>.
- [16] C. Barton, J. Mixson, Noise transmission and control for a light twin-engine aircraft, *J. Aircraft* 18 (7) (1981) 570–575. doi:<https://doi.org/10.2514/3.57528>.
- [17] C. Maury, P. Gardonio, S. J. Elliott, Active control of the flow-induced noise transmitted through a panel, *AIAA J.* 39 (10) (2001) 1860–1867. doi:<https://doi.org/10.2514/2.1200>.
- 765 [18] R. Camussi, Noise sources in turbulent shear flows: fundamentals and applications, Vol. 545, Springer Science & Business Media, Vienna, 2013.
- [19] M. Strasberg, D. Feit, Vibration damping of large structures induced by attached small resonant structures, *J. Acoust. Soc. Am.* 99 (1) (1996) 335–344. doi:<https://doi.org/10.1121/1.414545>.
- 770 [20] A. Akay, Z. Xu, A. Carcaterra, I. M. Koç, Experiments on vibration absorption using energy sinks, *J. Acoust. Soc. Am.* 118 (5) (2005) 3043–3049. doi:<https://doi.org/10.1121/1.2046767>.
- [21] I. M. Koç, A. Carcaterra, Z. Xu, A. Akay, Energy sinks: vibration absorption by an optimal set of undamped oscillators, *J. Acoust. Soc. Am.* 118 (5) (2005) 3031–3042. doi:<https://doi.org/10.1121/1.2074807>.
- 775 [22] A. Carcaterra, A. Akay, C. Bernardini, Trapping of vibration energy into a set of resonators: Theory and application to aerospace structures, *Mech. Syst. Sig. Process.* 26 (2012) 1–14. doi:<https://doi.org/10.1016/j.ymsp.2011.05.005>.
- [23] J. Vignola, A. Glean, J. Judge, T. Ryan, Optimal apparent damping as a function of the bandwidth of an array of vibration absorbers, *J. Acoust. Soc. Am.* 134 (2) (2013) 1067–1070. doi:<https://doi.org/10.1121/1.4812777>.
- 780 [24] L. Brillouin, Wave propagation in periodic structures: electric filters and crystal lattices, Vol. 2, Dover publications, Mineola, 1953.
- [25] Z. Liu, X. Zhang, Y. Mao, Y. Zhu, Z. Yang, C. T. Chan, P. Sheng, Locally resonant sonic materials, *Science* 289 (5485) (2000) 1734–1736. doi:<https://doi.org/10.1126/science.289.5485.1734>.
- 785 [26] P. Sheng, X. Zhang, Z. Liu, C. T. Chan, Locally resonant sonic materials, *Physica B* 338 (1-4) (2003) 201–205. doi:[https://doi.org/10.1016/S0921-4526\(03\)00487-3](https://doi.org/10.1016/S0921-4526(03)00487-3).
- [27] C. Goffaux, J. Sánchez-Dehesa, A. L. Yeyati, P. Lambin, A. Khelif, J. Vasseur, B. Djafari-Rouhani, Evidence of fano-like interference phenomena in locally resonant materials, *Phys. Rev. Lett.* 88 (22) (2002) 225502. doi:<https://doi.org/10.1103/PhysRevLett.88.225502>.
- 790 [28] P. Celli, S. Gonella, Heterogeneity meets disorder: anomalous wave transport in telescopic metamaterials, arXiv (2017). doi:<https://doi.org/10.48550/arXiv.1703.08522>.
- [29] D. Mead, Wave propagation in continuous periodic structures: research contributions from southamp-

- ton, 1964–1995, *J. Sound Vib.* 190 (3) (1996) 495–524. doi:<https://doi.org/10.1006/jsvi.1996.0076>.
- [30] M. I. Hussein, Reduced bloch mode expansion for periodic media band structure calculations, *Proc. R. Soc. London, Ser. A* 465 (2109) (2009) 2825–2848. doi:<https://doi.org/10.1098/rspa.2008.0471>. 795
- [31] T.-T. Wu, Z.-G. Huang, T.-C. Tsai, T.-C. Wu, Evidence of complete band gap and resonances in a plate with periodic stubbed surface, *Appl. Phys. Lett.* 93 (11) (2008) 111902. doi:<https://doi.org/10.1063/1.2970992>.
- [32] J. Jung, H.-G. Kim, S. Goo, K.-J. Chang, S. Wang, Realisation of a locally resonant metamaterial on the automobile panel structure to reduce noise radiation, *Mech. Syst. Sig. Process.* 122 (2019) 206–231. doi:<https://doi.org/10.1016/j.ymssp.2018.11.050>. 800
- [33] A. Hall, G. Dodd, E. Calius, Diffuse field measurements of locally resonant partitions, in: *ACOUSTICS 2017, Auckland, New Zealand, Vol. 2017, 2017*.
- [34] N. de Melo Filho, C. Claeys, E. Deckers, W. Desmet, Metamaterial foam core sandwich panel designed to attenuate the mass-spring-mass resonance sound transmission loss dip, *Mech. Syst. Sig. Process.* 139 (2020) 106624. doi:<https://doi.org/10.1016/j.ymssp.2020.106624>. 805
- [35] T. Wang, M. Sheng, Q. Qin, Sound transmission loss through metamaterial plate with lateral local resonators in the presence of external mean flow, *J. Acoust. Soc. Am.* 141 (2) (2017) 1161–1169. doi:<https://doi.org/10.1121/1.4976194>. 810
- [36] W. De Roeck, W. Desmet, Experimental acoustic identification of flow noise sources in expansion chambers, in: *ISMA 2008, Leuven, Belgium, Vol. 1, Katholieke Universiteit Leuven, Departement Werktuigkunde; Leuven, 2008, pp. 455–470*.
- [37] P. Welch, The use of fast fourier transform for the estimation of power spectra: a method based on time averaging over short, modified periodograms, *IEEE Trans. Audio Electroacoust.* 15 (2) (1967) 70–73. doi:<https://doi.org/10.1109/TAU.1967.1161901>. 815
- [38] W. Heylen, S. Lammens, P. Sas, et al., *Modal analysis theory and testing, Vol. 200, Katholieke Universiteit Leuven, Belgium, 1997*.
- [39] R. King, A review of vortex shedding research and its application, *Ocean Eng.* 4 (3) (1977) 141–171. doi:[https://doi.org/10.1016/0029-8018\(77\)90002-6](https://doi.org/10.1016/0029-8018(77)90002-6). 820
- [40] C. Williamson, Oblique and parallel modes of vortex shedding in the wake of a circular cylinder at low reynolds numbers, *Tech. rep., California Inst of Tech Pasadena Graduate Aeronautical Labs (1989)*. doi:<https://doi.org/10.1017/S0022112089002429>.
- [41] C. Williamson, R. Govardhan, A brief review of recent results in vortex-induced vibrations, *J. Wind Eng. Ind. Aerodyn.* 96 (6-7) (2008) 713–735. doi:<https://doi.org/10.1016/j.jweia.2007.06.019>. 825
- [42] C. Norberg, Flow around a circular cylinder: aspects of fluctuating lift, *J. Fluids Struct.* 15 (3-4) (2001) 459–469. doi:<https://doi.org/10.1006/jfls.2000.0367>.
- [43] A. Dewan, *Tackling turbulent flows in engineering, Springer Science & Business Media, Berlin, Heidelberg, 2010*.
- [44] M. Amabili, S. Carra, Thermal effects on geometrically nonlinear vibrations of rectangular plates with fixed edges, *J. Sound Vib.* 321 (3-5) (2009) 936–954. doi:<https://doi.org/10.1016/j.jsv.2008.10.004>. 830
- [45] N. Siemens, *Nastran 12. quick reference guide, Siemens PLM Software Inc (2017)*.
- [46] R. L. Clark, K. D. Frampton, Aeroelastic structural acoustic coupling: Implications on the control of turbulent boundary-layer noise transmission, *J. Acoust. Soc. Am.* 102 (3) (1997) 1639–1647. doi:<https://doi.org/10.1121/1.420075>. 835
- [47] K. D. Frampton, R. L. Clark, Sound transmission through an aeroelastic plate into a cavity, *AIAA J.* 35 (7) (1997) 1113–1118. doi:<https://doi.org/10.2514/2.221>.
- [48] P. Vitiello, S. De Rosa, F. Franco, Convected field analysis of flat panels response to turbulent boundary layer induced excitation, *Aerosp. Sci. Technol.* 12 (1) (2008) 91–104. doi:<https://doi.org/10.1016/j.ast.2007.10.003>. 840
- [49] E. Ciappi, S. De Rosa, F. Franco, P. Vitiello, M. Miozzi, On the dynamic behavior of composite panels under turbulent boundary layer excitations, *J. Sound Vib.* 364 (2016) 77–109. doi:<https://doi.org/10.1016/j.jsv.2016.03.019>.

- //doi.org/10.1016/j.jsv.2015.11.024.
- 845 [50] C. C. Claeys, K. Vergote, P. Sas, W. Desmet, On the potential of tuned resonators to obtain low-frequency vibrational stop bands in periodic panels, *J. Sound Vib.* 332 (6) (2013) 1418–1436. doi:  
https://doi.org/10.1016/j.jsv.2012.09.047.
- [51] C. Claeys, N. G. R. de Melo Filho, L. Van Belle, E. Deckers, W. Desmet, Design and validation of  
850 metamaterials for multiple structural stop bands in waveguides, *Extreme Mech. Lett.* 12 (2017) 7–22.  
doi:https://doi.org/10.1016/j.eml.2016.08.005.
- [52] J. J. Wijker, *Spacecraft structures*, Springer Science & Business Media, 2008.
- [53] F. Pires, C. Claeys, E. Deckers, W. Desmet, The impact of resonant additions' footprint on the stop  
band behavior of 1d locally resonant metamaterial realizations, *J. Sound Vib.* 491 (2021) 115705.  
doi:https://doi.org/10.1016/j.jsv.2020.115705.
- 855 [54] N. de Melo Filho, L. Van Belle, C. Claeys, E. Deckers, W. Desmet, Dynamic mass based sound transmission loss prediction of vibro-acoustic metamaterial double panels applied to the mass-air-mass resonance, *J. Sound Vib.* 442 (2019) 28–44. doi:https://doi.org/10.1016/j.jsv.2018.10.047.
- [55] Y. Xiao, J. Wen, X. Wen, Flexural wave band gaps in locally resonant thin plates with periodically  
860 attached spring–mass resonators, *J. Phys. D: Appl. Phys.* 45 (19) (2012) 195401. doi:https://doi.org/10.1088/0022-3727/45/19/195401.
- [56] P. G. Domadiya, E. Manconi, M. Vanali, L. V. Andersen, A. Ricci, Numerical and experimental investigation of stop-bands in finite and infinite periodic one-dimensional structures, *J. Vib. Control* 22 (4) (2016) 920–931. doi:https://doi.org/10.1177/1077546314537863.
- [57] C. Sugino, S. Leadham, M. Ruzzene, A. Erturk, On the mechanism of bandgap formation in locally  
865 resonant finite elastic metamaterials, *J. Appl. Phys.* 120 (13) (2016) 134501. doi:https://doi.org/10.1063/1.4963648.
- [58] D. Beli, J. Arruda, M. Ruzzene, Wave propagation in elastic metamaterial beams and plates with interconnected resonators, *Int. J. Mech. Sci.* 139 (2018) 105–120. doi:https://doi.org/10.1016/j.ijsolstr.2018.01.027.
- 870 [59] H. Peng, P. F. Pai, Acoustic metamaterial plates for elastic wave absorption and structural vibration suppression, *Int. J. Mech. Sci.* 89 (2014) 350–361. doi:https://doi.org/10.1016/j.ijmecsci.2014.09.018.
- [60] C. Sugino, M. Ruzzene, A. Erturk, Merging mechanical and electromechanical bandgaps in locally resonant metamaterials and metastructures, *J. Mech. Phys. Solids* 116 (2018) 323–333. doi:https://doi.org/10.1016/j.jmps.2018.04.005.
- 875 [61] S. El-Borgi, R. Fernandes, P. Rajendran, R. Yazbeck, J. Boyd, D. Lagoudas, Multiple bandgap formation in a locally resonant linear metamaterial beam: Theory and experiments, *J. Sound Vib.* 488 (2020) 115647. doi:https://doi.org/10.1016/j.jsv.2020.115647.
- [62] P. F. Pai, Metamaterial-based broadband elastic wave absorber, *J. Intell. Mater. Syst. Struct.* 21 (5) (2010) 517–528. doi:https://doi.org/10.1177/1045389X09359436.
- 880 [63] P. F. Pai, H. Peng, S. Jiang, Acoustic metamaterial beams based on multi-frequency vibration absorbers, *Int. J. Mech. Sci.* 79 (2014) 195–205. doi:https://doi.org/10.1016/j.ijmecsci.2013.12.013.
- [64] L. Cremer, M. Heckl, B. Petersson, S.-B. S.-S. *Vibrations, Sound radiation at audio frequencies* (2005).
- [65] C. C. Claeys, P. Sas, W. Desmet, On the acoustic radiation efficiency of local resonance based stop  
885 band materials, *J. Sound Vib.* 333 (14) (2014) 3203–3213. doi:https://doi.org/10.1016/j.jsv.2014.03.019.
- [66] D. Mead, S. Parthan, Free wave propagation in two-dimensional periodic plates, *J. Sound Vib.* 64 (3) (1979) 325–348. doi:https://doi.org/10.1016/0022-460X(79)90581-9.